Understanding the Promotional Effect of Mn_2O_3 on Micro-/Mesoporous Hybrid Silica Nanocubic-Supported Pt Catalysts for the Low-Temperature Destruction of Methyl Ethyl Ketone: An Experimental and Theoretical Study

Chi He,[*,†,‡] Zeyu Jiang,[†] Mudi Ma,[†] Xiaodong Zhang,[§] Mark Douthwaite,[‡] Jian-Wen Shi,[*,∥] and Zhengping Hao[⊥]

[†]Department of Environmental Science and Engineering, State Key Laboratory of Multiphase Flow in Power Engineering, School of Energy and Power Engineering, Xi'an Jiaotong University, Xi'an 710049, Shaanxi, People's Republic of China

[‡]Cardiff Catalysis Institute, School of Chemistry, Cardiff University, Main Building, Park Place, Cardiff CF10 3AT, U.K.

[§]Department of Environmental Science and Engineering, School of Environment and Architecture, University of Shanghai for Science and Technology, Shanghai 200093, People's Republic of China

[∥]Center of Nanomaterials for Renewable Energy, State Key Laboratory of Electrical Insulation and Power Equipment, School of Electrical Engineering, Xi'an Jiaotong University, Xi'an 710049, Shaanxi, People's Republic of China

[⊥]National Engineering Laboratory for VOCs Pollution Control Material & Technology, University of Chinese Academy of Sciences, Beijing 101408, People's Republic of China

[*] Supporting Information

ABSTRACT: $Pt_{0.3}Mn_x/SiO_2$ nanocubic (nc) micro-/meso-porous composite catalysts with varied Mn contents were synthesized and tested for the oxidation of methyl ethyl ketone (MEK). Results show that MEK can be efficiently decomposed over synthesized $Pt_{0.3}Mn_x/SiO_2$-nc materials with a reaction rate and turnover frequency respectively higher than 12.7 mmol g_{Pt}^{-1} s^{-1} and 4.7 s^{-1} at 100 °C. Among these materials, the $Pt_{0.3}Mn_5/SiO_2$-nc catalyst can completely oxidize MEK at just 163 °C under a high space velocity of 42600 mL g^{-1} h^{-1}.

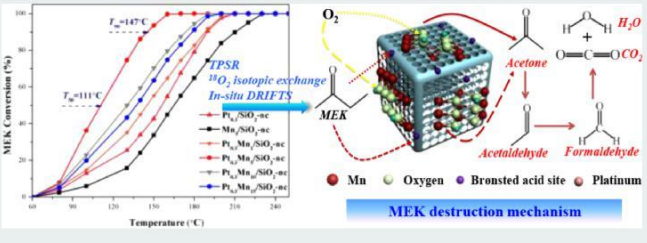

The remarkable performance of these catalysts is attributed to a synergistic effect between the Pt nanoparticles and Mn_2O_3. NH_3-TPD and NH_3-FT-IR experiments revealed that exposed Mn_2O_3 (222) facets enhance the quantity of Brønsted acid sites in the catalyst, which are considered to be responsible for promoting the desorption of surface-adsorbed O_2 and CO_2. It is suggested that the desorption of these species liberates active sites for MEK molecules to adsorb and react. $^{18}O_2$ isotopic labeling experiments revealed that the presence of a Pt−O−Mn moiety weakens the Mn−O bonding interactions, which ultimately promotes the mobility of lattice oxygen in the Mn_2O_3 system. It was determined that the Mn^{4+}/Mn^{3+} redox cycle in Mn_2O_3 allows for the donation of electrons to the Pt nanoparticles, enhancing the proportion of Pt^0/Pt^{2+} and in turn increasing the activity and stability of catalyst. In situ DRIFTS, online FT-IR, and DFT studies revealed that acetone and acetaldehyde are the main intermediate species formed during the activation of MEK over the $Pt_{0.3}Mn_5/SiO_2$-nc catalyst. Both intermediates were found to partake in sequential reactions resulting in the formation of H_2O and CO_2 via formaldehyde.

KEYWORDS: micro-/mesoporous composite nanocubic silica, Pt−Mn bimetallic center, methyl ethyl ketone, catalytic oxidation, DFT calculation, activation mechanism

INTRODUCTION

Volatile organic compounds (VOCs) are major contributors to air pollution and are extremely damaging to human health due to the formation of photochemical smog and secondary aerosols, in addition to their general carcinogenicity.[1] One such VOC, methyl ethyl ketone (MEK), is used in a number of industrial applications and classified as an oxygenated volatile organic compound (OVOC). Given that these compounds are so hazardous, it is crucial that reliable and efficient methods be developed for their disposal. The complete catalytic oxidation of VOCs into CO_2 and water is one such method and is especially useful for removing low concentration of VOCs (<0.5 vol %) from waste streams.[2] There are two different approaches to catalyst design presented in the current literature: the application of supported noble-metal catalysts and that of transition metal oxide catalysts.[3] Both types of

catalysts possess their own specific advantages; however, supported noble-metal catalysts are perhaps considered to be most promising for the total oxidation of VOCs due to their high specific activity, resistance to deactivation, and ability to be regenerated.[4] Among them, platinum-supported catalysts have been extensively studied for the total oxidation of OVOCs due to their superb catalytic efficiency.

Current drives to improve the performance of supported noble-metal-based catalysts for catalytic oxidation is predominantly focused toward increasing the dispersion of the metal particles, reducing the loading of the noble metals used, and varying the preparation method and/or metal precursor.[5,6] Investigations into the application of single-site noble-metal catalysts are limited, which is likely due to the difficulties associated with their synthesis, susceptibility to poisoning by S/ Cl, and proneness to sintering at high reaction temperatures.[7] Interestingly, noble-metal and transition-metal cosupported catalysts have been found to be more active and stable for VOC destruction than materials containing single noble-metal active sites.[8] It has been reported previously that introducing transition-metal oxides into supported noble-metal catalysts can enhance their catalytic activity due to synergistic effects between the multicomponent metal phases.[9] The transition-metal oxides are reported to increase the performance of these materials by enhancing the activation of oxygen and instigating a change in the physicochemical properties of the noble-metal active sites.[9] For instance, Qu et al. [8] recently showed that AgCo/APTES@MCM-41 (Ag/Co = 3/1) could completely decompose formaldehyde at temperatures as low as 90 °C, while only a 30% decomposition was achieved over a Ag/ APTES@MCM-41 catalyst under the same reaction conditions. Additionally, Cui et al.[10] revealed that the activity of a Pt/Al_2O_3 catalyst could be significantly enhanced through the incorpo-ration of FeO_x for the oxidation of formaldehyde. This increased performance was attributed to the formation of surface Pt−O−Fe species.

The properties of the support material and transition-metal oxide have been found to have a significant effect on the performance of these noble-metal catalysts. Boaro and co-workers, for example, showed that increasing the surface area of the support material increased the dispersion of the noble-metal particles.[11] As such, many studies investigating the hierarchical effect of silica supports with different surface areas have been carried out to find supports for noble-metal-based catalysts.[12,13] In our previous work, we found that the activity of Pd/SC (SC denotes short column SBA-15) catalysts was proportional to the volume of the support micropores for the oxidation of toluene.[12] For this reason, it is rational to expect that micro-/ mesoporous hybrid silica materials would be an ideal support material for noble- and transition-metal cosupported catalysts, given that one would expect these materials to possess sufficiently high porosities to achieve a good noble-metal dispersion and promote the diffusion rates for reactants and products in a given reaction. Furthermore, we also confirmed that the morphology of the support can have a significant effect on the catalytic activity of these materials, which could further influence the approach invoked for the design of these materials.[13]

The type of transition-metal oxides used in these composite catalysts has also been investigated for the total oxidation of VOCs. Scirè and Liotta[14] concluded that a $Au/CoO_x/Al_2O_3$ catalyst was significantly more active for the oxidation of C_3H_6 than $Au/MnO_x/Al_2O_3$ and $Au/FeO_x/Al_2O_3$ catalysts. Transition-metal oxides in these composite catalysts can act as cocatalysts in this system, which can enhance the redox properties and introduce surface defects at the gold/oxide interfaces. Other reports have shown that manganese oxides are catalytically active for the total oxidation of VOCs such as propane, n-hexane, benzene, and toluene.[15] The influence of MnO_x on noble-metal supported catalysts in total oxidation reactions has attracted a great deal of attention due to its low volatility and ability to easily bind and release oxygen. Arias et al.[16] investigated the performance of MnO_x/Al_2O_3, Pd/Al_2O_3, and $Pd\text{-}MnO_x/Al_2O_3$ catalysts for the oxidation of methanol. The $Pd\text{-}MnO_x/Al_2O_3$ catalyst was found to exhibit a much higher activity and thermal stability in comparison to the corresponding MnO_x/Al_2O_3 and Pd/Al_2O_3 catalysts. Colman-Lerner et al.[17] showed that the activity of Pt/Mn/B is much higher than that of the corresponding Pt/B and Mn/B (B = bentonite monoliths) materials for the oxidation of toluene due to synergetic effects between Pt and Mn. The enhancement in activity was suggested to be related to the presence of Mn^{3+}/ Mn^{4+} species. Other works have correlated the catalytic performance of MnO_x to exposed facets on the materials surface. Xie et al.[18] studied the total oxidation of propane over nanosized MnO_2 particles with α, β, γ, and δ crystal phases and revealed that the activity of these catalysts varied in the order $\alpha\text{-}MnO_2 > \gamma\text{-}MnO_2 > \beta\text{-}MnO_2 > \delta\text{-}MnO_2$, which have (310), (120), (110), and (001) exposed facets, respectively. It was suggested that the presence of translational motion in the $\alpha\text{-}MnO_2$ phase and its stronger deformation and stretching modes were responsible for its better catalytic activity in the oxidation of propane.[18]

The catalytic oxidation of MEK over a $PdO_x\text{-}MnO_x/Al_2O_3$ catalyst was investigated by Arzamendi and co-workers.[19] In this study, it was revealed that the temperature for the complete oxidation of MEK was as high as 320 °C over a 1.0 wt % $PdO_x\text{-}MnO_x/Al_2O_3$ catalyst. High noble-metal loadings, inferior MEK activation capabilities, low CO_2 selectivity, and the production of hazardous byproducts have so far limited the application of these types of catalysts industrially. Pt-Mn-based catalysts supported on micro-/mesoporous hybrid silica have yet to be trialed as catalysts for the oxidation of OVOCs. In this work, Pt- and Mn-codecorated nanocubic silica (SiO_2-nc) catalysts with large specific surface areas and uniform 3D micro-/ mesoporous hybrid structures were synthesized. A promotional effect is observed for the oxidation of MEK when Mn_2O_3 is deposited onto a Pt/SiO_2-nc material. We found that the exposed (222) facets of Mn_2O_3 enhance the quantity and strength of the Brønsted acid sites in the catalyst, thereby promoting the mobility of lattice oxygen in the catalyst. It is also proposed that the presence of Mn^{4+}/Mn^{3+} redox cycle in Mn_2O_3 oxide facilitates the movement of electrons to and from the Pt metal particles, which increases the ratio of Pt^0/Pt^{2+} species present on the surface, ultimately increasing the stability of the catalyst. In addition to this, the MEK destruction routes and surface mechanism over $Pt_{0.3}Mn_x/SiO_2$-nc catalysts were proposed, which were based on results from in situ DRIFTS, TPSR, $^{18}O_2$ isotopic experimentation, and DFT experiments/ calculations.

EXPERIMENTAL SECTION

Catalyst Preparation. The synthesis of the nanocubic silica support was based on an approach used initially by Stöber but was later modified by Zhao et al.[20] For this, 1.0 g of cetyltrimethylammonium bromide (CTAB) was dissolved in

160 mL of deionized water with stirring. An 8.0 mL portion of a concentrated ammonia−water solution (25 wt %) was subsequently added, forming a clear solution. A mixture of tetraethoxysilane (TEOS) and n-hexane was then added to this solution dropwise over 40 min with continuous stirring, and the temperature of the solution was maintained at 30 °C, forming a homogeneous milky colloidal solution. The solution was stirred for another 12 h, after which the product was collected by centrifugation and washed with deionized water and ethanol. The final SiO_2-nc material was obtained by vacuum drying and calcining at 550 °C for 4 h in air with a ramp rate of 1 °C min^{-1}.

Polyvinylpyrrolidone (PVP)-capped Pt nanoparticles with a mean particle size of ca. 2 nm were synthesized by an ethylene glycol reduction method. For this, 20 mL of aqueous NaOH (0.25 M) was added to a 20 mL solution containing ethylene glycol-$H_2PtCl_6 \cdot 6H_2O$ (0.22 g) and was stirred at room temperature for 1 h, yielding a transparent yellow suspension. The mixture was subsequently heated at 90 °C for 2 h under a flow of N_2, resulting in the formation of a dark brown transparent homogeneous colloidal solution of Pt nanoparticles. The Pt nanoparticles were subsequently precipitated from the addition of about 2−3 mL of a 2 M HCl solution (dropwise until pH 3−4), which was subsequently collected by centrifugation and dispersed in ethanol containing 112 mg of PVP (K. 30). A proportion of the Pt NPs and manganous acetate were subsequently added to 70 mL of ethanol with stirring for 30 min, after which the solution turned gray. The SiO_2-nc support was then added to this solution with stirring and ultrasonication for an additional 5 h. After filtering, washing, and calcining at 500 °C for 4 h, the final catalysts were obtained and denoted as $Pt_{0.3}Mn_x/SiO_2$-nc (x represents the content of Mn).

Catalyst Characterizations. The synthesized samples were systematically characterized by X-ray diffraction (XRD), low-temperature N_2 adsorption−desorption, inductively coupled plasma optical emission spectrometry (ICP-OES), hydrogen and oxygen titration (HOT), field emission scanning electron microscopy (FE-SEM), high-resolution transmission electron microscopy (HR-TEM), high-angle annular dark-field imaging in scanning transmission electron microscopy (HAADF-STEM), Fourier transform infrared spectroscopy (FT-IR), ultraviolet−visible spectroscopy adsorption spectra (UV−vis), ^{29}Si magic angle spinning nuclear magnetic resonance (^{29}Si MAS NMR), X-ray photoelectron spectroscopy (XPS), oxygen temperature-programmed desorption (O_2-TPD), CO_2 temper-ature-programmed desorption (CO_2-TPD), NH_3 temperature-programmed desorption (NH_3-TPD), FT-IR spectroscopy for NH_3 adsorption (NH_3-IR), FT-IR spectroscopy for CO adsorption (CO-IR), temperature-programmed isotopic ex-change (TPIE), and TGA-FT-IR analysis. The detailed methods for each technique are described in the Supporting Information.

Catalytic Activity. The performance of each material for MEK oxidation was investigated in a continuous-flow fixed-bed reactor consisting of a steel tube (6 mm i.d.) at atmospheric pressure. In each test, 0.3 g of catalyst (40−60 mesh) was placed into the tube reactor. Prior to testing, the catalyst was pretreated at 200 °C with N_2 for 1 h. The MEK feed (800 ppm) was generated by using a N_2 bubbler in a thermostatic bath at 35 °C and mixing with air (79% N_2 + 21% O_2). The total flow rate was maintained at 212 mL min^{-1} (space velocity 42600 mL g^{-1} h^{-1}). The catalyst bed was subsequently set to the desired temperature and left to equilibrate for 30 min before online sampling was initiated. The concentrations of MEK, CO, and CO_2 were measured by an online gas chromatograph (GC-9890B; Linghua, China) equipped with a flame ionization detector (FID) and HT-Wax column (30 m × 0.32 mm (i.d.) × 0.5 μm). The conversion of MEK (X_{MEK}) was calculated as shown by eq 1

$$X_{MEK}\ (\%) = \frac{[MEK]_{in} - [MEK]_{out}}{[MEK]_{in}} \times 100\% \quad (1)$$

where $[MEK]_{in}$ and $[MEK]_{out}$ represent the MEK concentrations in the inlet and outlet gas, respectively.

The CO_2 selectivity (S_{CO_2}) was calculated as shown by eq 2

$$S_{CO_2}\ (\%) = \frac{[CO_2]_{out}}{4[MEK]_{in} X_{MEK}} \times 100\% \quad (2)$$

where $[CO_2]_{out}$ is the CO_2 concentrations in the outlet gas.

The reaction rate (r_{MEK}, mmol g_{Pt}^{-1} s^{-1}) was calculated as shown by eq 3

$$r_{MEK} = \frac{X_{MEK} V_{MEK}}{W_{cat}(wt\ \%\ Pt)} \quad (3)$$

where W_{cat} represents the catalyst weight (g), wt % Pt is the content of Pt in the catalyst (%), and V_{MEK} is the MEK gas flow rate (mol s^{-1}).

When the conversion of MEK is <15%, a dependence of the reaction rate (r_{MEK}) on the products of CO_2 and H_2O may be ignored and the empirical kinetic expression of the reaction rate equation of MEK oxidation can be described as shown by eq 4:

$$r_{MEK} = A \exp\left(-\frac{E_a}{RT}\right) P_{MEK}^{\alpha} P_{O_2}^{\beta} \quad (4)$$

From the natural logarithm of eq 4, eq 5 can be obtained:

$$\ln r = \ln A + \alpha \ln P_{MEK} + \beta \ln P_{O_2} - E_a/RT \quad (5)$$

The components of the reactant gas feed undergo minor changes during the kinetics data testing, and the conversion of MEK is <15%. Therefore, ln A, α ln P_{MEK}, and β ln P_{O_2} can be supposed to be approximately constant, and eq 5 can be simplified to eq 6:

$$\ln r = -\frac{E_a}{RT} + C \quad (6)$$

The activation energy (E_a) can be obtained from the slope of the resulting linear plot of ln r versus 1/T.

The turnover frequency based on the Pt nanoparticles (TOF_{Pt}, s^{-1}) was calculated as shown by eq 7[21,22]

$$TOF_{Pt} = \frac{X_{MEK} V_{MEK} N_A}{W_{cat}(wt\ \%\ Pt) D_{Pt}} \quad (7)$$

where N_A is Avogadro's constant and D_{Pt} represents the dispersion of Pt nanoparticles on catalysts (%).

Reaction Route Determination. Temperature-pro-grammed surface reaction (TPSR) experiments were conducted in air (20% O_2) and in N_2, respectively. For these, 0.3 g of catalyst (40−60 mesh) was loaded into a U-type quartz tube of Builder PCA-1200. Prior to analysis, the catalyst was pretreated in an air flow (40 mL min^{-1}) at 400 °C for 1 h and then cooled to room temperature (25 °C). A 800 ppm amount of MEK diluted by air (100 mL min^{-1}) was introduced into the reaction system, and an adsorption−desorption equilibrium was

Table 1. Textural Properties of All Synthesized Catalysts

sample	Pt content[a] (wt %)	Pt dispersion[b] (%)	S_{BET}[c] ($m^2\ g^{-1}$)	V_{pore}[d] ($cm^3\ g^{-1}$)	V_{micro}[e] ($cm^3\ g^{-1}$)	V_{micro}/V_{pore} (%)	d_{pore}[f] (nm)
SiO_2-nc			970.5	1.12	0.42	38	3.6
$Pt_{0.3}/SiO_2$-nc	0.31	49.7	836.1	0.82	0.35	43	3.4
Mn_5/SiO_2-nc			751.4	0.80	0.32	40	3.5
$Pt_{0.3}Mn_1/SiO_2$-nc	0.28	53.1	809.9	0.79	0.35	44	3.3
$Pt_{0.3}Mn_5/SiO_2$-nc	0.27	59.6	803.4	0.92	0.35	38	3.8
$Pt_{0.3}Mn_{10}/SiO_2$-nc	0.25	52.9	811.7	0.78	0.34	44	3.4
$Pt_{0.3}Mn_{15}/SiO_2$-nc	0.29	57.2	772.0	0.81	0.33	41	3.5

[a]Actual Pt content detected by ICP-OES. [b]Dispersion of Pt estimated by HOT. [c]Specific surface area obtained at $P/P_0 = 0.05-0.30$. [d]Total pore volume estimated at $P/P_0 = 0.99$. [e]Micropore volume estimated from the t-plot method. [f]BJH pore diameter calculated from the desorption branch.

achieved. The reactor was subsequently heated from 50 to 550 °C at a ramp rate of 5 °C min^{-1} in air (40 mL min^{-1}). Signals corresponding to CO_2 (m/z 44) and formaldehyde (m/z 29) were monitored and recorded online using a Sunny Hengping SHP8400PMS-L mass spectrometer.

$^{18}O_2$ isotopic studies were conducted using a PCA-1200 instrument. For this, 0.3 g of catalyst was pretreated in a pure N_2 flow (40 mL min^{-1}) at 400 °C for 1 h and then cooled to room temperature (25 °C). A MEK gas mixture with 2 vol % $^{18}O_2/N_2$ (Isotec, Lianhong, China, 97 atom % ^{18}O) was subsequently injected and maintained for 20 min. Following this, the temperature of the catalyst bed was increased to 300 °C at a rate of 5 °C min^{-1} and maintained for 10 min. All three oxygen isotopic species, namely $C^{18}O_2$ (m/z 48), $C^{16}O^{18}O$ (m/z 46), and $C^{16}O_2$ (m/z 44) were continuously monitored online using a SHP8400PMS-L mass spectrometer.

In situ DRIFTS of MEK oxidation was performed using a Bruker Tensor 37 infrared spectrometer, equipped with a mercury cadmium telluride (MCT) detector cooled by liquid nitrogen. A Harrick reaction cell was fitted with KBr windows and connected to a purging and adsorption gas control system. The total flow rate was controlled by a mass flow meter. Prior to the catalytic oxidation of MEK, the catalyst samples were pretreated under N_2 at 500 °C for 1 h to remove the surface impurities. In each case, a spectrum corresponding to the catalyst powder was recorded at selected reaction temperatures under an N_2 flow. This spectrum was then subtracted from the corresponding spectrum of the catalyst and reaction mixture in the cell. For the MEK oxidation experiment, the catalysts were exposed to a gas mixture consisting of 800 ppm MEK/20% O_2/ N_2 at temperatures in the range of 80−240 °C. The system reached a steady state in about 20−25 min, as verified by the stabilized MS peak intensities. All spectra were collected at a resolution of 4 cm^{-1} with 100 scans.

DFT Studies. Crystalline Mn_2O_3 and noncrystalline SiO_2 surfaces were constructed and immobilized with a Pt cluster. The vacuum space was set to be 15 Å, which is considered to be sufficient to avoid interaction between the two neighboring images. The reactants, intermediates, and products were added onto the surface of each model substrate. The first-principles calculations in the framework of the density functional theory were carried out using the Cambridge Sequential Total Energy Package (CASTEP). The exchange-correlation function under the generalized gradient approximation (GGA) with norm-conserving pseudopotentials and Perdew−Burke−Ernzerhof functional was adopted to describe the electron−electron interactions. An energy cutoff of 750 eV was used, and a k-point sampling set of 5 × 5 × 1 was tested to be converged. A force tolerance of 0.01 eV $Å^{-1}$, energy tolerance of 5.0×10^{-7} eV per atom, and maximum displacement of 5.0×10^{-4} Å were considered. Each atom in the storage models was allowed to relax to the minimum enthalpy without any constraints.

The adsorption energy E_{ads} of A (A = reactants, intermediates, and products) group on the surface of substrates was defined as

$$E_{ads} = E_{*A} - (E_{*} + E_{A}) \quad (8)$$

where *A and * denote the adsorption of A onto the substrates and the bare substrates and E_A denotes the energy of the A group.

RESULTS

Structural and Textual Properties. The powder X-ray diffraction patterns associated with each of the synthesized materials are displayed in Figure S1. The diffraction peak at $2\theta = 23.1°$, which is observed in the diffraction patterns of all the materials, can be assigned to the amorphous silica support.[12] With the exception of the Mn_5/SiO_2-nc material, all of the materials have three diffraction peaks at $2\theta = 40.1$, 46.4, and 67.6°, which correspond to the (111), (200), and (220) planes of metallic Pt, respectively.[23] In comparison to the $Pt_{0.3}/SiO_2$-nc material, the characteristic Pt diffractions become weaker with the $Pt_{0.3}Mn_x/SiO_2$-nc materials, which suggests that the dispersion of Pt on the surface is improved by the introduction of manganese oxide, in agreement with other previous observations.[24] Interestingly, no diffraction peaks that are characteristic of manganese oxide are observed in any of the materials, suggesting that the Mn, when present in this materials, is likely to also be well dispersed.

The N_2 adsorption−desorption isotherms of the synthesized micro-/mesoporous nanocubic silica exhibit a type IV isotherm, with a large and clear H2 hysteresis loop (Figure S2A).[25] The sharp increase at $P/P_0 < 0.1$ in the adsorption isotherm of SiO_2-nc material indicates that there is a large quantity of micropores present. A clear condensation step at relative pressure (P/P_0) ranges of 0.4−0.8 indicates that there are uniform framework-confined mesopores also present in the material.[26] The average pore diameter, total pore volume, and BET specific surface area of the SiO_2-nc material were determined to be ca. 3.6 nm, 1.12 $cm^3\ g^{-1}$, and 970.5 $m^2\ g^{-1}$, respectively (Figure S2B and Table 1). Interestingly, large amounts of micropores with an average pore volume of 0.42 $cm^3\ g^{-1}$ are also detected, which is indicative of a defined porosity of the SiO_2-nc support (Table 1). After this material is loaded with Pt and/or Mn, the specific surface area (751.4−836.1 $m^2\ g^{-1}$), total pore volume (0.78− 0.82 $cm^3\ g^{-1}$), and micropore volume (0.32−0.35 $cm^3\ g^{-1}$) all decrease slightly. Perhaps most noticeable is the correlating reduction in the specific surface area when increasing quantities of Mn are added to the material. This indicates that the Mn

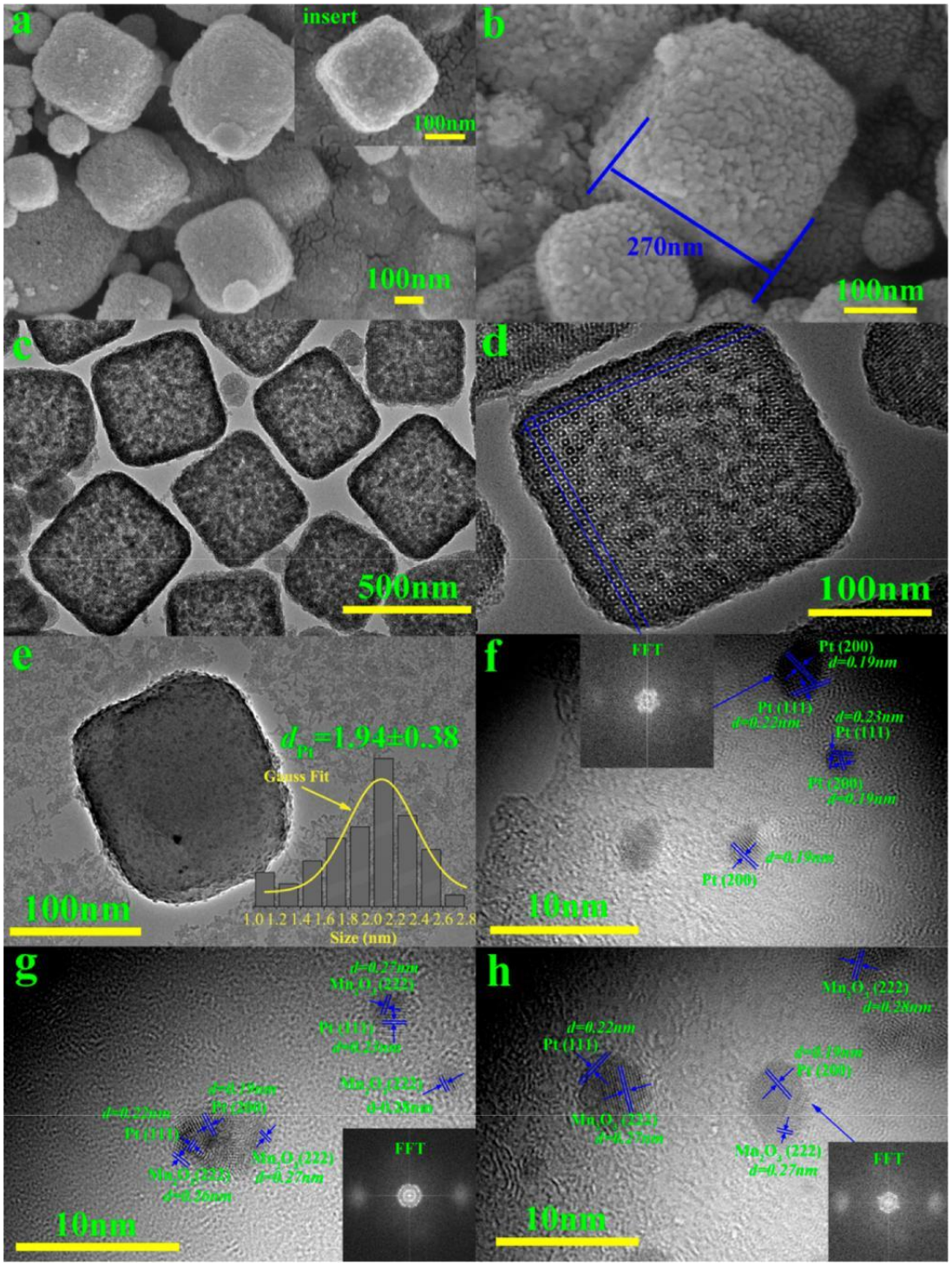

Figure 1. FE-SEM (a, b) and HR-TEM (c, d) images of SiO_2-nc and HR-TEM images of (e, g, h) $Pt_{0.3}Mn_5/SiO_2$-nc and (f) $Pt_{0.3}/SiO_2$-nc.

phases likely have a strong influence on the pore structure of these materials.

FE-SEM and HR-TEM images corresponding to the supported SiO_2-nc materials are displayed in Figure 1. From Figure 1a,b, it is evident that the SiO_2-nc support occupies a uniform nanocubic morphology (side length of ca. 270 nm) with defined edges and corners. The TEM images (Figure 1c,d) offer a more detailed insight into the pore distribution of the SiO_2-nc support. A highly ordered 3D porous structure is clearly observed in the SiO_2-nc material, with an average pore size of approximately 3 nm, which aligns with the results derived from the N_2 adsorption study (Figure S2 and Table 1). From Figure 1e, the average size of the Pt nanoparticles in the $Pt_{0.3}Mn_5/SiO_2$-nc material was found to be 1.94 ± 0.38 nm, indicating a uniform, well-defined particle size distribution (59.6%, Table 1) of Pt particles. Figure 1f shows two different lattice planes with spacing of 0.19 and 0.22 nm over $Pt_{0.3}/SiO_2$-nc, which correspond to the (220) and (111) planes of metallic Pt, respectively. From Figure 1g,h, it is clear that the Pt atoms coordinate with the Mn_2O_3 (222) facets, which are approximately 10−20 nm in size. To confirm this, the Pt atoms on the Mn_2O_3 (222) facets were examined using higher

magnifications (Figure 1g,h). From these additional images, it can be concluded that the Pt nanoparticles preferentially occupy over the (222) facet of the Mn_2O_3. HAADF-STEM (Figure S3a) characterization was subsequently used to probe the surface of the $Pt_{0.3}Mn_5/SiO_2$-nc material. From this image, it is clear that there is a highly ordered mesoporous structure present in the material and that the Pt nanoparticles appear to be homogeneously dispersed on the surface. Additional EDS mapping images of O, Mn, and Pt in the $Pt_{0.3}Mn_5/SiO_2$-nc sample are shown in Figure S3b−d. These reveal that there is a uniform distribution of O, Mn, and Pt throughout the material.

Properties and Composition. ^{29}Si solid-state MAS NMR (Figure 2A) was subsequently used to probe the unit structure of the SiO_2-nc and $Pt_{0.3}Mn_5/SiO_2$-nc materials. For both of these materials, the main peak observed is at a chemical shift of approximately −111 ppm and can be attributed to tetrahedral Si with four Si neighbors (i.e.,$Si(OSi)_4$)[27] and is indicative of the asymmetric stretching of the Si−O−Si from silicon−oxygen tetrahedral species. Interestingly, this peak is noticeably less intense in the ^{29}Si solid-state NMR of the $Pt_{0.3}Mn_5/SiO_2$-nc material. As such, it can be concluded that the introduction of Mn_2O_3 balances the electronegativity of the SiO_2-nc support, thereby weakening the Si−O interaction, which is considered to be beneficial for enhancing the stability of the catalyst.

The FT-IR spectra of all of the synthesized materials are displayed in Figure 2B. The transmission peaks at approximately 3745 and 3635 cm^{-1} can be attributed to the surface silanol groups, which appear to interact weakly with adsorbed water over the silica surface.[28] The small feature at around 3289 cm^{-1} can be assigned to the stretching and bending vibrations of surface hydroxyls.[29] The surface hydroxyls also give rise to a band of δ(Si−OH) and ν(Si−OH) at 1633 cm^{-1}.[30] With regard to the framework of the materials, the intense and broad band observed at approximately 1083 cm^{-1} can be ascribed to the asymmetric stretching of the Si−O−Si moiety in the silicon− oxygen tetrahedral species. A weak band corresponding to the symmetric stretching of this moiety is observed at 810 cm^{-1}, which aligns with the results of ^{29}Si MAS NMR (Figure 2A).[31] The band observed at 458 cm^{-1} is attributed to symmetric stretching vibrations and tetrahedral Si−O bending modes.[28] The band at 3289 cm^{-1} corresponds to the stretching of the Mn−O moiety in the Mn_2O_3 phase, which becomes stronger with an increase in Mn content.

The coordination geometry of Pt and Mn_2O_3 in the various materials was investigated by UV−vis absorption spectroscopy, the corresponding spectra of which are displayed in Figure 2C. The band at approximately 241 nm can likely be attributed to O^{2-}-Mn^{3+},[32] which is indicative of charge transfer transitions of trivalent manganese ions in tetrahedral coordination geo-metries. This band could be assigned to the strong bonding of oxygen ligands to Mn^{3+} ions. The intensity of these bands is enhanced proportionally with an increase in Mn content in the material. Interestingly, there is a band at 304 nm in the $Pt_{0.3}$/ SiO_2-nc sample which appears to shift toward lower energies after the incorporation of Mn into the material. This shift is attributed to the formation of a Mn−O−Pt moiety.[33] The intensity of the characteristic peak at approximately 461 nm is ascribed to Pt−O−Mn moieties, which is enhanced with an increase in Mn_2O_3.[34] This suggests that, when Mn is present, Pt may interact with Mn_2O_3 (222) facets via conjugated π bonding, yielding Mn−O−Pt moieties. This would facilitate electron transfers from Mn to Pt and ultimately increase the

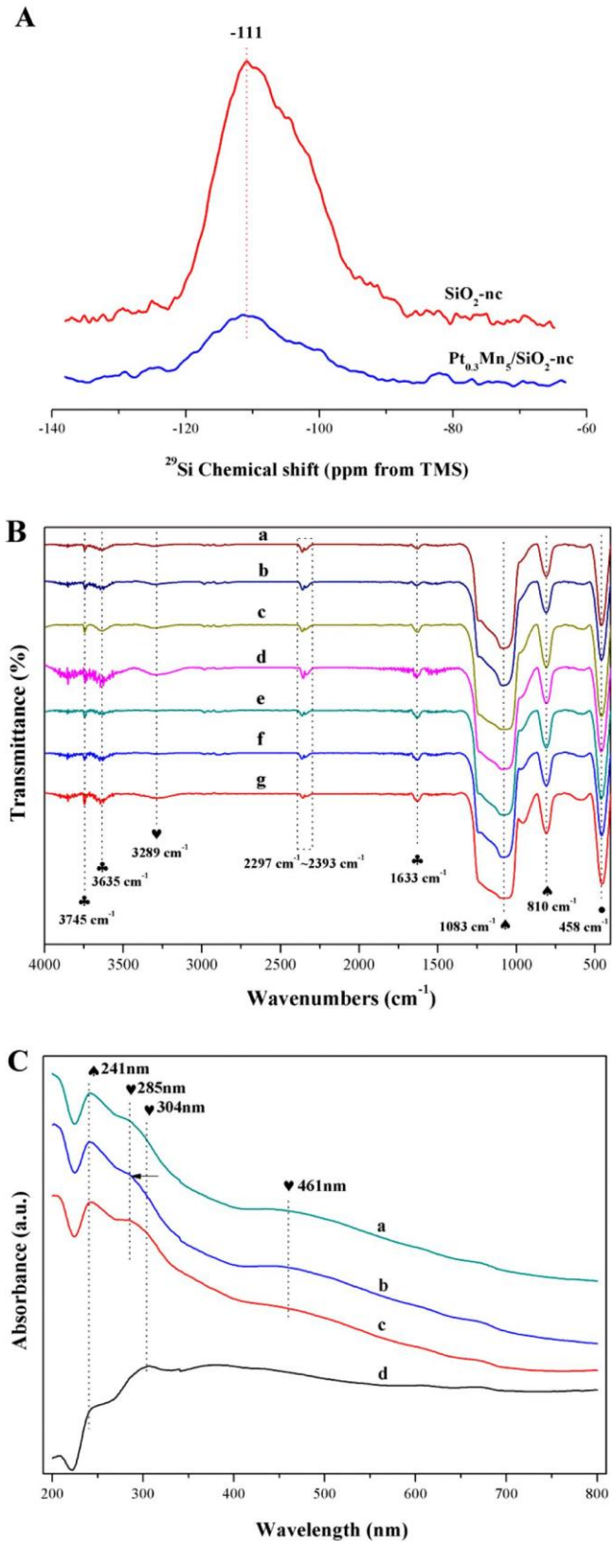

Figure 2. (A) ^{29}Si MAS NMR of SiO_2-nc support and $Pt_{0.3}Mn_5/SiO_2$-nc catalyst. (B) FT-IR spectra of (a) $Pt_{0.3}Mn_1/SiO_2$-nc, (b) $Pt_{0.3}Mn_5/SiO_2$-nc, (c) $Pt_{0.3}Mn_{10}/SiO_2$-nc, (d) $Pt_{0.3}Mn_{15}/SiO_2$-nc, (e) $Pt_{0.3}/SiO_2$-nc, (f) SiO_2-nc support, and (g) Mn_5/SiO_2-nc. (C) UV−vis absorption spectra of (a) $Pt_{0.3}Mn_{10}/SiO_2$-nc, (b) $Pt_{0.3}Mn_5/SiO_2$-nc, (c) $Pt_{0.3}Mn_1$/ SiO_2-nc, and (d) $Pt_{0.3}/SiO_2$-nc.

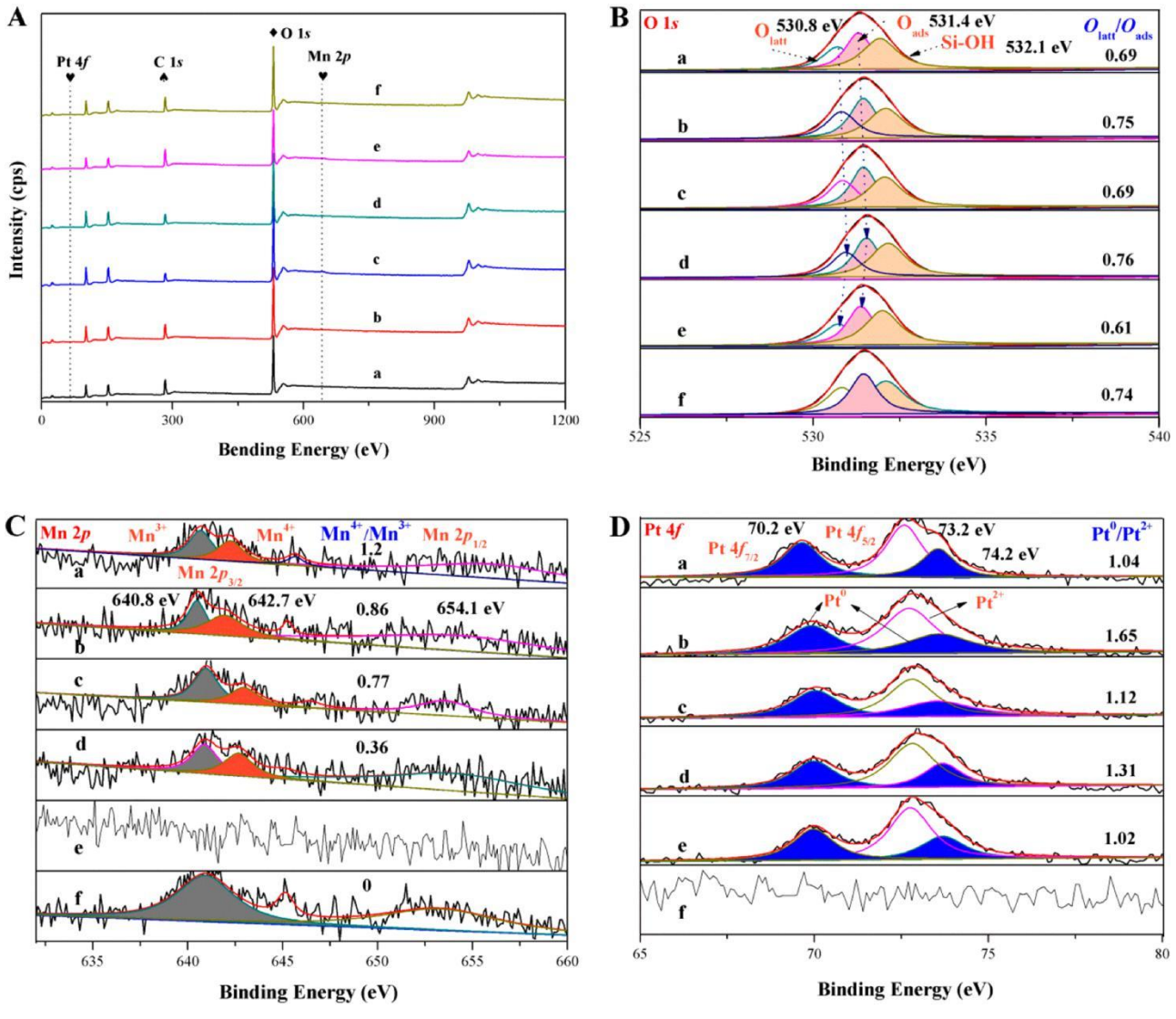

Figure 3. XPS spectra of (a) $Pt_{0.3}Mn_1/SiO_2$-nc, (b) $Pt_{0.3}Mn_5/SiO_2$-nc, (c) $Pt_{0.3}Mn_{10}/SiO_2$-nc, (d) $Pt_{0.3}Mn_{15}/SiO_2$-nc, (e) $Pt_{0.3}/SiO_2$-nc, and (f) Mn_5/SiO_2-nc: (A) survey scan of XPS spectra; (B) O 1s; (C) Mn 2p; (D) Pt 4f.

Pt^0/Pt^{2+} ratio, which could promote the oxidation of MEK molecules.

X-ray photoelectron spectroscopy (XPS) experiments were carried out to identify the chemical states of the surface O, Pt, and Mn in each of the prepared materials. The corresponding spectra are displayed in Figure 3. The C 1s and O 1s peaks are clear, while signals corresponding to the Mn 2p and Pt 4f states are very weak by comparison. The O 1s XPS spectra (Figure 3B) for all of the materials can be deconvoluted into three peaks with binding energies (BE) centered at approximately 532.1, 531.4, and 530.8 eV. These peaks can be assigned to oxygen associated with Si−OH (silanol group), surface-adsorbed O_2, and lattice oxygen, respectively.[35,36] Increasing the Mn content in the material leads to a high-energy shift in the peaks attributed to surface-adsorbed oxygen and lattice oxygen. This indicates that the introduction of Mn_2O_3 has a fairly substantial effect on the distribution of oxygen in the material. It is known that, with certain catalysts, lattice oxygen can have a significant influence on catalytic performance for the oxidation of VOCs.[35] Quantification of the peaks attributed to lattice oxygen (O_{latt}) and surface-adsorbed oxygen (O_{ads}) provided some interesting results. The O_{latt}/O_{ads} ratio for the $Pt_{0.3}/SiO_2$-nc material was calculated to be 0.61, which is noticeably lower than the O_{latt}/O_{ads} ratio calculated for the Mn_5/SiO_2-nc material (0.74). For the $Pt_{0.3}Mn_5/SiO_2$-nc material, the O_{latt}/O_{ads} ratio increased to 0.75, which is higher than that of $Pt_{0.3}Mn_1/SiO_2$-nc (0.69) and $Pt_{0.3}Mn_{10}/SiO_2$-nc (0.69) samples. The high O_{latt}/O_{ads} ratio ensures the superior catalytic performance of $Pt_{0.3}Mn_5/SiO_2$-nc for total oxidation of VOCs. As shown in Figure 3C, the Mn 2p XPS spectra can be split into Mn $2p_{3/2}$ and Mn $2p_{1/2}$.[37] The asymmetrical Mn $2p_{3/2}$ spectra can be deconvoluted into two components centered at BE values of 640.8 and 642.7 eV, which are characteristic of surface Mn^{3+} and Mn^{4+} species, respectively.[37] Interestingly, only one peak is observed in the Mn $2p_{3/2}$ region of the Mn_5/SiO_2-nc at 640.9 eV, which corresponds to the Mn^{3+} species. This suggests that, with this material, Mn is likely to only be present as Mn_2O_3. However, the peaks at binding energies which are characteristic of Mn^{4+} species appear in the XPS spectra of the $Pt_{0.3}Mn_x/SiO_2$ materials, suggesting that the Pt and Mn in the materials form Pt−O−Mn moieties. It is has previously been reported that Mn^{4+} species are highly active in VOC oxidation[38] and, as such, the Mn^{4+}/Mn^{3+} ratio could provide insights into the catalytic activities of these materials.

Table 2. Catalytic Performance of All Catalysts

sample	T_5[a] (°C)	T_{50}[a] (°C)	T_{90}[a] (°C)	r_v[b] (mmol g_{Pt}^{-1} s^{-1})	TOF_{Pt}[c] (s^{-1})	E_a[d] (kJ mol^{-1})	C_{wp}[e]
$Pt_{0.3}/SiO_2$-nc	80	156	190	10.2	4.0	55.04	2.17×10^{-3}
Mn_5/SiO_2-nc	93	165	210				
$Pt_{0.3}Mn_1/SiO_2$-nc	79	145	188	12.7	4.7	48.88	2.70×10^{-3}
$Pt_{0.3}Mn_5/SiO_2$-nc	72	111	147	32.9	10.7	41.36	6.99×10^{-3}
$Pt_{0.3}Mn_{10}/SiO_2$-nc	75	130	175	21.8	8.1	48.56	4.63×10^{-3}
$Pt_{0.3}Mn_{15}/SiO_2$-nc	80	138	179	16.8	5.7	61.12	3.57×10^{-3}

[a]Temperatures at 5%, 50%, and 90% conversion of MEK. [b]Reaction rate of MEK molecules transformed per surface area per unit time of various catalysts at 100 °C. [c]Turnover frequency based on the dispersion of Pt obtained at 100 °C. [d]Apparent activation energy obtained from Arrhenius plots. [e]Parameter calculated according to the Weisz−Prater criterion.

For this reason, the proportion of Mn^{4+}/Mn^{3+} present in each material was quantified and the ratios determined were as follows: Mn_5/SiO_2-nc (0) < $Pt_{0.3}Mn_{15}/SiO_2$-nc (0.36) < $Pt_{0.3}Mn_{10}/SiO_2$-nc (0.77) < $Pt_{0.3}Mn_5/SiO_2$-nc (0.86) < $Pt_{0.3}Mn_5/SiO_2$-nc (1.2). Figure 3D highlights how the asymmetrical Pt 4f peak can be deconvoluted into peaks representative of the Pt $4f_{7/2}$ and Pt $4f_{5/2}$ species. The peaks with BE energies of 70.2 and 74.2 eV are attributed to Pt^0, and the peak at a BE value of 73.24 eV can be assigned to Pt^{2+}.[29,30] As discussed previously, the Pt^0 species is highly active and plays an important role in VOC combustion.[3] From Figure 3D it is clear that the incorporation of Mn into these materials significantly enhances the proportion of Pt^0/Pt^{2+}. We believe that this is due to the transfer of electrons from Mn^{3+} to Pt^{2+}. In addition to this, the Pt^0/Pt^{2+} ratio in the $Pt_{0.3}Mn_5/SiO_2$-nc material (1.65) is much higher than that observed in $Pt_{0.3}/SiO_2$-nc (1.02).

Catalytic Performance. Values for the Weisz−Prater (C_{WP}) criterion for all the catalysts are shown in Table 2, and the maximum value is on the order of 10^{-3}.[22] As such, both the external and internal diffusional effects on the catalytic performance can be ignored. The catalytic behaviors of each of the materials for the oxidation of MEK were studied, and parameters such as MEK conversion temperature, destruction rate, activation energy, and turnover frequency were calculated and are displayed in Figure 4 and Table 2. Over the Mn_5/SiO_2-nc and $Pt_{0.3}/SiO_2$-nc catalysts, MEK is fully converted at 230 and 200 °C, respectively (Figure 4A), indicating that the Pt sites are more active than the Mn sites for the oxidation of MEK. Interestingly, the activity for MEK oxidation is greatly enhanced over the $Pt_{0.3}Mn_x/SiO_2$-nc catalysts, suggesting that introducing Mn into the materials has a dramatic effect on the catalytic performance. The $Pt_{0.3}Mn_5/SiO_2$-nc catalyst exhibited the highest catalytic activity, with approximately 90% of the MEK converted at 147 °C. To the best of our knowledge, this is the most promising active catalyst to date for the conversion of MEK at low temperature (Table S1). Sanz et al. had previously reported that a highly active 1.0 wt % Pt/OMS-2 catalyst could achieve 50% and 90% of MEK destruction at 170 and 190 °C, respectively, under a flow rate of 500 mL min^{-1}. In view of the specified reaction conditions, e.g., space velocities and noble-metal content, the $Pt_{0.3}Mn_5/SiO_2$-nc catalyst also has its advantages over some of other types of catalysts. For instance, the GHSV in this work is 42600 mL g^{-1} h^{-1} or 25440 h^{-1}; the 0.5 wt % Pd-Ce/ZSM-5 catalyst exhibits inferior activity (T_{50} of 210 °C, T_{90} of 225 °C) for MEK oxidation with a similar space velocity (28000 h^{-1}). Taking the CO_2 yield as a value, T_{50} (139 °C), T_{90} (161 °C), and E_a (41.3 kJ mol^{-1}) of our $Pt_{0.3}Mn_5/SiO_2$-nc catalyst are lower than those (T_{50} = 190 °C and T_{90} = 205 °C based on CO_2 yield) over Pt/NaX with GHSV of 15300 h^{-1} and those over 1.0 wt % Pd−Mn/Al_2O_3 with GHSV of 425 h^{-1} (T_{50} = 290 °C, T_{90} = 305 °C, and E_a = 117 kJ mol^{-1} based on CO_2 yield).

The CO_2 selectivity observed over three of the synthesized catalysts ($Pt_{0.3}Mn_5/SiO_2$-nc, $Pt_{0.3}/SiO_2$-nc, and Mn_5/SiO_2-nc) were also assessed, the results from which are displayed in Figure 4B. The CO_2 selectivity was highest for $Pt_{0.3}Mn_5/SiO_2$-nc, with 100% selectivity to CO_2 observed at only 210 °C. The $Pt_{0.3}/SiO_2$-nc and Mn_5/SiO_2-nc required much higher reaction temperatures in order to achieve the same CO_2 selectivity (250 and 260 °C, respectively). Interestingly, a sudden drop is observed in the CO_2 selectivity associated with the $Pt_{0.3}/SiO_2$-nc between 210 and 230 °C. This abnormality was not observed in the selectivity data associated with the $Pt_{0.3}Mn_5/SiO_2$-nc and Mn_5/SiO_2-nc, which may be attributed to sufficient lattice oxygen being present in these materials. Nevertheless, these selectivity data provide further evidence that the exposed Mn_2O_3 (222) facets accelerate the MEK oxidation process.

The stability of these catalysts is also an important parameter to consider for supported noble-metal catalysts, as the susceptibility of these to undergo thermal deactivation is often responsible for their limited industrial applications.[39,40] In order to determine whether these catalysts undergo thermal deactivation, an additional study was conducted where the performances of the $Pt_{0.3}Mn_5/SiO_2$-nc and $Pt_{0.3}/SiO_2$-nc catalysts were monitored for an extended amount of time. The results of this study are displayed in Figure 4C. Very little deactivation is observed with both materials, indicating that they possess excellent stability in the total oxidation of MEK.

As water is one of the reaction products and is also commonly found in industrial exhaust streams, it was important to determine whether it had a detrimental effect on the long-term oxidation behavior of the catalysts. Figure 4D illustrates how different concentrations of water vapor (3 and 5 vol %) affect the catalytic performance of these materials at 180 °C. Water vapor was found to have a negative effect on the oxidation of MEK, which is likely to be due to the competitive adsorption of H_2O, MEK, and O_2 molecules on the catalyst surface. A loss in MEK conversion of ca. 27.7% and 32.0% is observed over the $Pt_{0.3}Mn_5/SiO_2$-nc and $Pt_{0.3}/SiO_2$-nc catalysts, respectively, when 5 vol % water vapor is introduced into the stream. Interestingly, when the water vapor was switched off, the conversion of MEK returned to the original values for $Pt_{0.3}Mn_5/SiO_2$-nc and $Pt_{0.3}/SiO_2$-nc catalysts within 45 and 65 min, respectively. A similar effect was observed when 3 vol % water vapor was introduced into the reaction stream; conversion dropped from 19.6% and 23% for the $Pt_{0.3}Mn_5/SiO_2$-nc and $Pt_{0.3}/SiO_2$-nc catalysts, respectively, but once again their activity returned within 30 and 45 min when the water

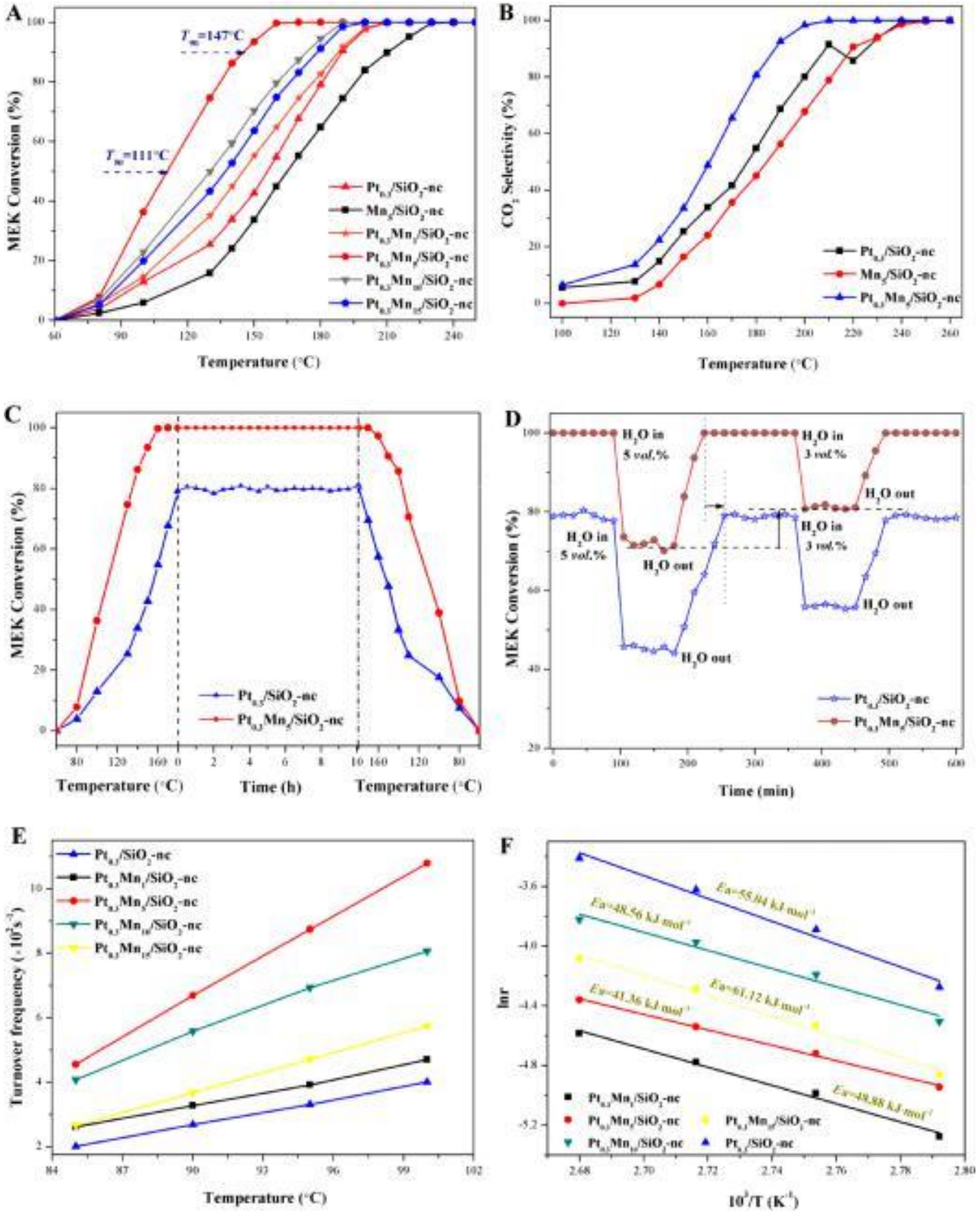

Figure 4. (A) Catalytic activity and (B) CO_2 selectivity of different catalysts for MEK combustion. (C) Stability test of active samples for MEK oxidation. (D) Effect of water vapor on MEK combustion at 180 °C. (E) Turnover frequency of active samples based on the dispersion of Pt. (F) Arrhenius plots of active samples for MEK catalytic oxidation.

vapor was switched off. Despite this detrimental effect on the catalytic performance, it is interesting that the $Pt_{0.3}Mn_5/SiO_2$-nc exhibited a smaller drop in conversion upon the addition of water in comparison to the $Pt_{0.3}/SiO_2$-nc catalyst. As discussed previously, Mn_2O_3 can balance the negative charge of the silica support and enhance the Brønsted acid sites on the catalyst, which are beneficial for producing more well dispersed Pt nanoparticles.[17] In addition to this, the Mn_2O_3 has the ability to

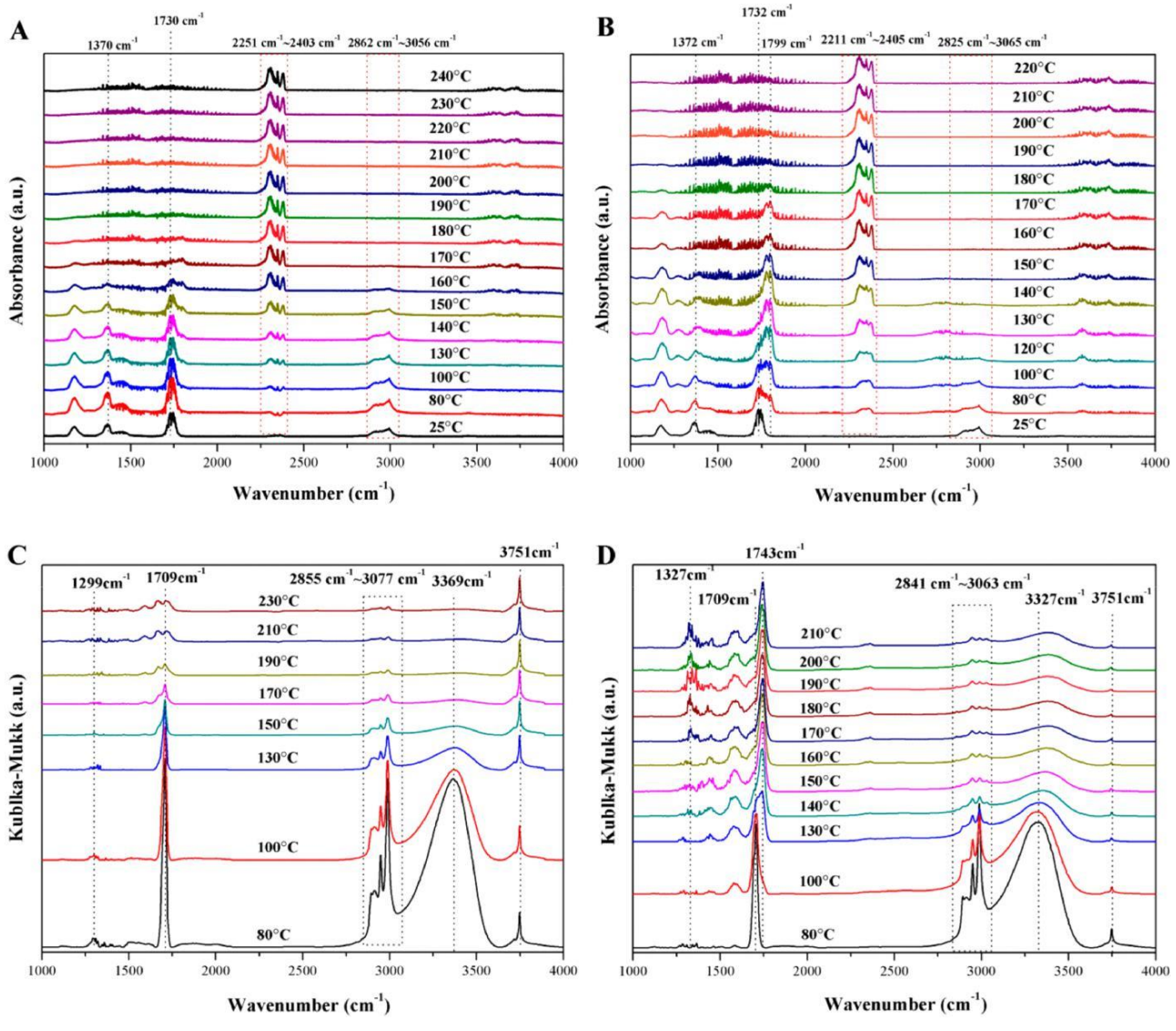

Figure 5. Online FT-IR spestra of outlet stream after MEK combustion over (A) $Pt_{0.3}/SiO_2$-nc and (B) $Pt_{0.3}Mn_5/SiO_2$-nc. In situ DRIFTS spectra of (C) $Pt_{0.3}/SiO_2$-nc and (D) $Pt_{0.3}Mn_5/SiO_2$-nc for MEK oxidation as a function of reaction temperature in flowing MEK + N_2 + O_2 from 80 to 230 °C.

transfer electrons to Pt active sites via the Mn−O−Pt moiety formation, which increases the Pt^0/Pt^{2+} ratio and enhances the interaction between active sites and support.[16] As such, catalysts with a higher proportion of Pt^0 and higher metal dispersion are likely to resist aggregation at high temperatures and maintain a better performance. It is possible that the Mn species reduce the adsorption of H_2O onto the catalyst surface, which ultimately liberates more adsorption sites for MEK molecules to adsorb. The reactivity data which highlight the superior stability of the $Pt_{0.3}Mn_5/SiO_2$-nc is supplemented by additional TGA-FT-IR, XRD, and FT-IR spectroscopy data of both the fresh and used $Pt_{0.3}Mn_5/SiO_2$-nc samples, which are displayed in Figure S4.

The turnover frequencies (TOFs) and activation energies can also be used to compare the activities of each catalyst. The TOF_{Pt} values were calculated from the quantity of Pt active sites on each catalyst and are displayed in Figure 4E. These data reveal that the TOF_{Pt} value of $Pt_{0.3}Mn_5/SiO_2$-nc for MEK oxidation is 2−3 times higher than that observed over $Pt_{0.3}/SiO_2$-nc material. The highest TOF_{Pt} value was observed over the $Pt_{0.3}Mn_5/SiO_2$-nc material (10.79 s^{-1} at 100 °C), demonstrating its excellent low-temperature activity for MEK destruction. The calculated TOF_{Pt} value for catalytic decomposition of MEK at 100 °C decreases in the sequence $Pt_{0.3}Mn_5/SiO_2$-nc (10.79 s^{-1}) > $Pt_{0.3}Mn_{10}/SiO_2$-nc (8.07 s^{-1}) > $Pt_{0.3}Mn_{15}/SiO_2$-nc (5.74 s^{-1}) > $Pt_{0.3}Mn_1/SiO_2$-nc (4.70 s^{-1}) > $Pt_{0.3}/SiO_2$-nc (4.00 s^{-1}) (Table 2). The results confirm that $Pt_{0.3}Mn_x/SiO_2$-nc species are clearly excellent catalysts for the oxidation of MEK.

The activation energy (E_a) of MEK oxidation was subsequently used as an additional measure for comparing catalytic performance. For this, low MEK conversions (between 5 and 10%) was used to compare the low-temperature activity of each of the catalysts. Replotting the reaction data in an Arrhenius plot allows for the calculation of E_a values for each of the catalysts. The corresponding Arrhenius plots are displayed in Figure 4F, and corresponding data are shown in Table 2. The activation energies were found to increase according to the sequence $Pt_{0.3}Mn_5/SiO_2$-nc (41.36 kJ mol^{-1}) < $Pt_{0.3}Mn_{10}/SiO_2$-nc (48.56 kJ mol^{-1}) < $Pt_{0.3}Mn_1/SiO_2$-nc (48.88 kJ mol^{-1}) < $Pt_{0.3}/SiO_2$-nc (55.04 kJ mol^{-1}) < $Pt_{0.3}Mn_{15}/SiO_2$-nc (61.12 kJ mol^{-1}). The $Pt_{0.3}Mn_5/SiO_2$-nc catalyst was found to possess the

lowest E_a (41.36 kJ mol^{-1}), suggesting that MEK oxidation proceeds more readily over this material in comparison to the others which were tested.

MEK Destruction Mechanism. In addition to MEK, some of the byproducts which can form from the partial oxidation of the substrate can also be toxic and damaging to the environment. As such, it is crucially important that the mechanistic pathways for the decomposition of MEK are fully understood, so that these systems operate as close to a 100% CO_2 yield as possible.[18] In this study, we have already shown that Mn_2O_3 has a promotional effect on the Pt nanoparticles for the combustion of MEK. In situ DRIFTS experiments were subsequently conducted in order to provide information on the products distribution formed during the reaction. To supplement this, additional experiments were conducted at different temperatures using an online FT-IR for analysis.

Figure 5A,B shows the online FT-IR results of MEK oxidation over the $Pt_{0.3}/SiO_2$-nc and $Pt_{0.3}Mn_5/SiO_2$-nc catalysts, respectively. With the $Pt_{0.3}/SiO_2$-nc catalyst, a broad peak appears between 2862 and 3056 cm^{-1} at 25 °C which can be attributed to the $-CH_3$ group in MEK.[41] Another intense peak at 1730 cm^{-1} and a weakly intense peak at 1370 cm^{-1} are also observed, which can be attributed to the C O in MEK.[42,43] These peaks reduce in intensity as the temperature increases and completely disappear at 180 °C. Interestingly, bands characteristic of CO_2 vibrations (between 2251 and 2403 cm^{-1}) appear to gradually increase as the reaction temperature approaches 190 °C. This correlates with observations made in previous studies.[44] Interestingly, with the $Pt_{0.3}Mn_5/SiO_2$-nc catalyst, a new band at 1799 cm^{-1} appears at 80 °C and gradually increases when the temperature is increased, before reaching a maxima at 130 °C and then descending gradually. This peak corresponds to the vibration of a symmetric C O moiety from an intermediate species, which is not observed when the reaction is conducted over the $Pt_{0.3}/SiO_2$-nc catalyst.[45] It can therefore be concluded that the $Pt_{0.3}Mn_5/SiO_2$-nc catalyst offers an alternative mechanistic route to MEK combustion from that which occurs over the $Pt_{0.3}/SiO_2$-nc catalyst, where acetone is believed to be the main intermediate product. The characteristic peaks which are indicative of MEK (2825−3065, 1732, and 1372 cm^{-1}) decrease when the temperature increases and vanish at 150 °C, which coincides with the results from the activity tests (illustrated in Figure 4A). The vibration of CO_2 appears between 2211 and 2405 cm^{-1} and maximizes at 170 °C, which suggests that MEK is decomposed to CO_2 at 170 °C over the $Pt_{0.3}Mn_5/SiO_2$-nc catalyst (Figure 4B).

Similar conclusions can be drawn from the in situ DRIFTS experiments which were conducted over the $Pt_{0.3}/SiO_2$-nc and $Pt_{0.3}Mn_5/SiO_2$-nc catalysts. Once again, the DRIFTS spectra for each catalyst were assessed at different reaction temperatures with MEK flowing over the materials. The results of these experiments are displayed in Figure 5C,D. The sharp peak at 3751 cm^{-1} is attributed to the Brønsted acid sites of the catalyst.[43] Interestingly, with increasing temperature this peak remains unchanged for the $Pt_{0.3}/SiO_2$-nc material but a decrease in the intensity of this peak is observed with the $Pt_{0.3}Mn_5/SiO_2$-nc material with increasing temperature. As discussed previously, acid sites are essential for MEK combustion over $Pt_{0.3}Mn_5/SiO_2$-nc catalyst, as they provide a proton to break the conjugation and fracture the $-CH_3$ moiety. As such, the intensity of this peak is reduced as the reaction proceeds. With the $Pt_{0.3}/SiO_2$-nc catalyst (Figure 5C), the broad peak at 3369 cm^{-1} is attributed to hydroxyl groups which corresponds to 2-butanol, 2,3-butanediol, and adsorbed water.[43] The band at 1709 cm^{-1} is indicative of vibrational asymmetric C O species, which could be indicative of MEK, acetaldehyde, or formaldehyde.[42] The peak at 1299 cm^{-1} is attributed to vibrations from the $-CH_3$ species in MEK or acetaldehyde.[43] The bands also observed between 2855 and 3077 cm^{-1} may be attributed to the bending and stretching vibrations of C−H[41] and thus must correspond to residual adsorbed hydrocarbon species from the decomposition of MEK. A new bend at 1743 cm^{-1} which corresponds to the symmetric C O moiety in acetone can be detected in MEK oxidation over $Pt_{0.3}Mn_5/SiO_2$-nc[45] and proves that the Mn_2O_3 phase has a significant effect on the MEK reaction route and oxidation mechanism.

DISCUSSION

In this work, the promotional effect of Mn_2O_3 with highly exposed (222) planes on the performance of $Pt_{0.3}Mn_x/SiO_2$-nc micro-/mesoporous composite catalysts for the oxidation of MEK was investigated. It was determined that the Mn_2O_3 (222) facets increase the quantity of Brønsted acid sites in these materials, which promote the mobility of lattice oxygen. It is suggested that these increased Brønsted acid sites balance the negative charge of the support and accelerate the desorption of surface adsorbed O_2 and CO_2 (Figure S5).

The acidity of all the materials which were synthesized was evaluated by NH_3-TPD (Figure 6A) and NH_3-IR (Figure 6B). In Figure 6A, a small peak is observed at 195 °C for the SiO_2-nc support, which can be attributed to physisorbed NH_3.[46] The profiles of the $Pt_{0.3}Mn_1/SiO_2$-nc, fresh $Pt_{0.3}Mn_5/SiO_2$-nc, and used $Pt_{0.3}Mn_5/SiO_2$-nc materials were subsequently deconvoluted by the Gauss curve fitting method into two peaks, which correspond to physisorbed NH_3 (desorption peak at 173−194 °C) and ammonia adsorbed on Brønsted acid sites (desorption peak at 311−334 °C).[46] Interestingly, as the quantity of Mn_2O_3 in the material is increased, the desorption peak associated with ammonia adsorbed onto Brønsted acid sites increases to a higher temperature. Previous work has showed that such a shift is indicative of an increase in the strength of the acid sites.[47] The quantity of acid sites in each material was compared by examining the integrated areas of the corresponding NH_3 desorption peaks, an approach which has been used previously.[48] The areas of the NH_3 desorption peak for the $Pt_{0.3}Mn_1/SiO_2$-nc and $Pt_{0.3}Mn_5/SiO_2$-nc catalysts were determined to be 182 and 457, respectively, indicating that increasing the quantity of Mn_2O_3 in the material increases the quantity of Brønsted acid sites in the system. With the used $Pt_{0.3}Mn_5/SiO_2$-nc catalyst, the integrated area of the NH_3 desorption peak was reduced from 457 to 347, suggesting that some of the Brønsted acid sites are consumed during the combustion of MEK.

From the FT-IR spectra displayed in Figure 6B, it is clear that there are no characteristic peaks which can be attributed to the adsorption of NH_3 over the SiO_2-nc material. Interestingly, in the corresponding spectrum associated with the $Pt_{0.3}Mn_5/SiO_2$-nc material, bands appear at 1467 and 1673−1781 cm^{-1} which are indicative of the symmetric and asymmetric bending vibrations of NH^{4+} species on Brønsted acid sites.[48] An important observation to note is that the intensities of these bands are significantly lower in the corresponding spectrum of the used $Pt_{0.3}Mn_5/SiO_2$-nc catalyst. In conclusion, the NH_3-TPD and FT-IR experiments indicate that the presence of Mn_2O_3 in these catalysts increases the quantity and strength of

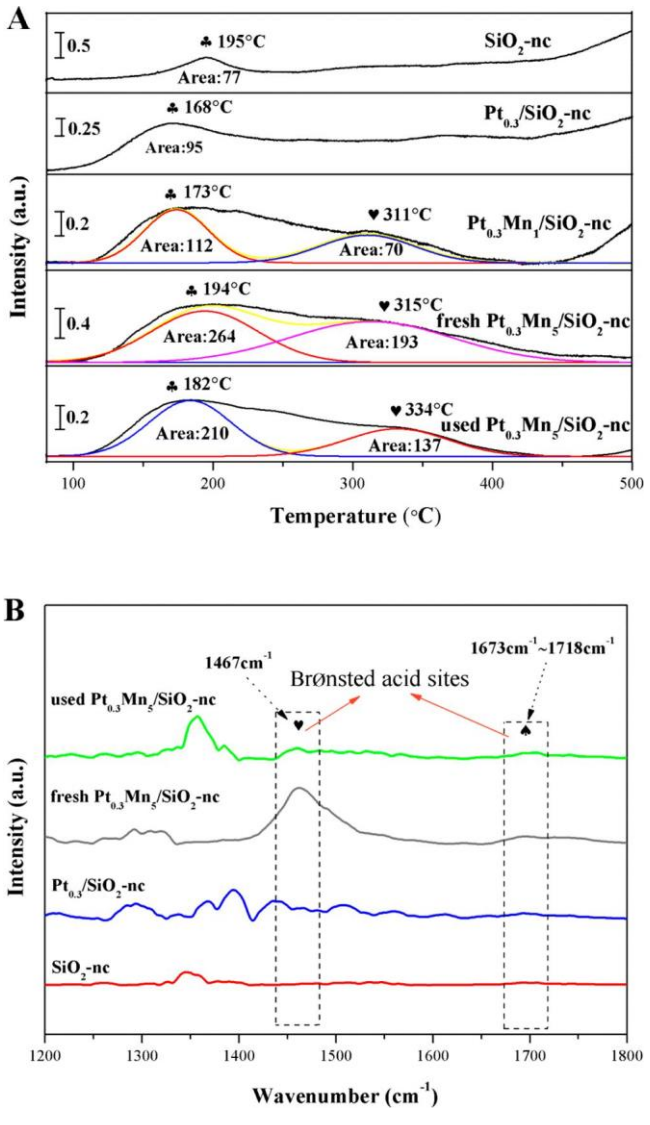

Figure 6. (A) NH_3-TPD profiles of active samples. (B) FT-IR spectra of various catalysts for NH_3 adsoprtion.

Brønsted acid sites over the materials. The Brønsted acid sites have been shown previously to significantly promote noble-metal dispersion and stability due to their electrophilic character.[49] As such, the adsorption of MEK on the catalysts' surface is enhanced (Figure S6).

Metallic Pt nanoparticles are considered to be critically important for the combustion of VOCs.[12] As such, additional studies were conducted in order to investigate whether reduced Pt sites were important for the oxidation of MEK. To do this, CO was used as a probe molecule to investigate the nature of the Pt active sites in each of the catalysts. Chemisorption studies using CO in this way can reveal detailed information on the chemical environment in close proximity to the Pt nanoparticle active sites.[50] It is known that, when CO adsorbs to Pt active sites, electrons are partially transferred from a d orbital of the metal to the antibonding CO molecular orbital. This electron transfer strengthens the Pt−C bond and weakens the C−O bond. Any strengthening of the Pt−CO bond typically correlates with an increase in the vibrational frequencies of the Pt−C bond.[51] As shown in Figure 7, bands corresponding to carbonates and CO_2 are observed at 1628 and 2344 cm^{-1}, respectively, which can be attributed to the oxidation of small quantities of the CO probe molecule by the Pt active sites; this is a phenomenon that has previously been attributed to the involvement of lattice oxygen.[52] The intensity of the CO_2 peak increases in the order $Pt_{0.3}/SiO_2$-nc < $Pt_{0.3}Mn_1/SiO_2$-nc < $Pt_{0.3}Mn_5/SiO_2$-nc, while the opposite trend is observed for the characteristic carbonate peak. Larger quantities of the CO probe molecule appear to be converted to CO_2 over the $Pt_{0.3}Mn_5/SiO_2$-nc material in comparison to that over the $Pt_{0.3}/SiO_2$-nc material. These results confirm that the $Pt_{0.3}Mn_x/SiO_2$-nc catalysts possess more lattice oxygen than the $Pt_{0.3}/SiO_2$-nc materials. For the $Pt_{0.3}Mn_1/SiO_2$-nc and $Pt_{0.3}Mn_5/SiO_2$-nc samples, a band at 2090 cm^{-1} is observed which can be assigned to bridge-bond CO which is absorbed on different terrace and step sites on the Pt nanoparticle.[53] This is characteristic of adsorbed CO on Pt (111) planes,[54] which suggests that a large proportion of the exposed Pt in these materials exists in the (111) plane. This observation is supported by the XRD diffraction patters displayed in Figure S1. Interestingly, in the spectrum associated with the $Pt_{0.3}/SiO_2$-nc material, the band corresponding to the adsorbed

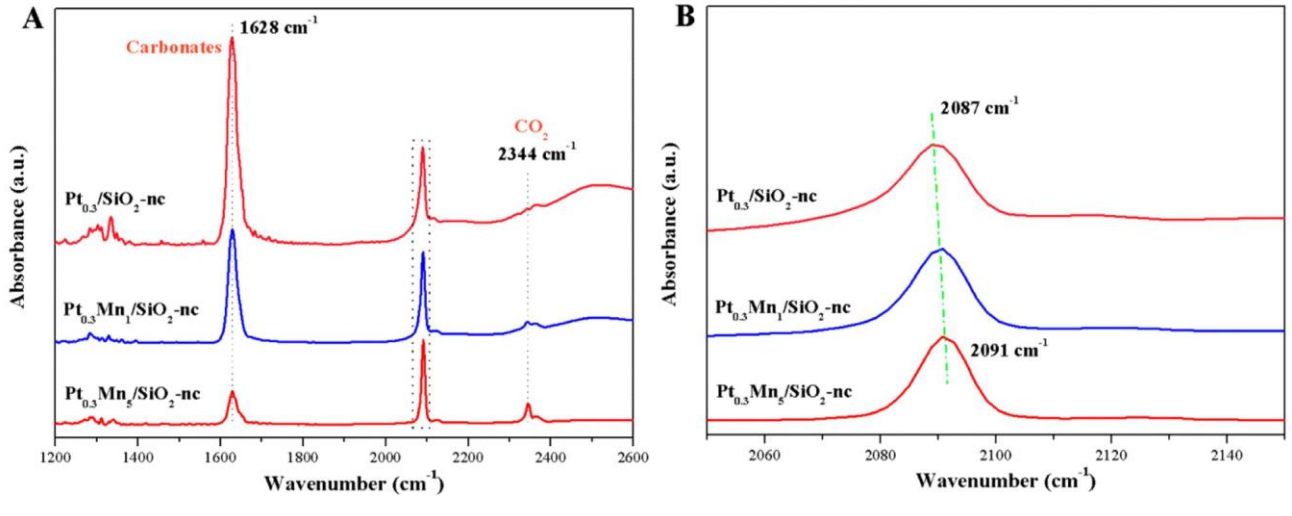

Figure 7. FT-IR spectra of typical catalysts for CO adsoprtion: (A) full spectrum analysis from 1200 to 2600 nm^{-1}; (B) magnification of region between 2050 and 2150 nm^{-1}.

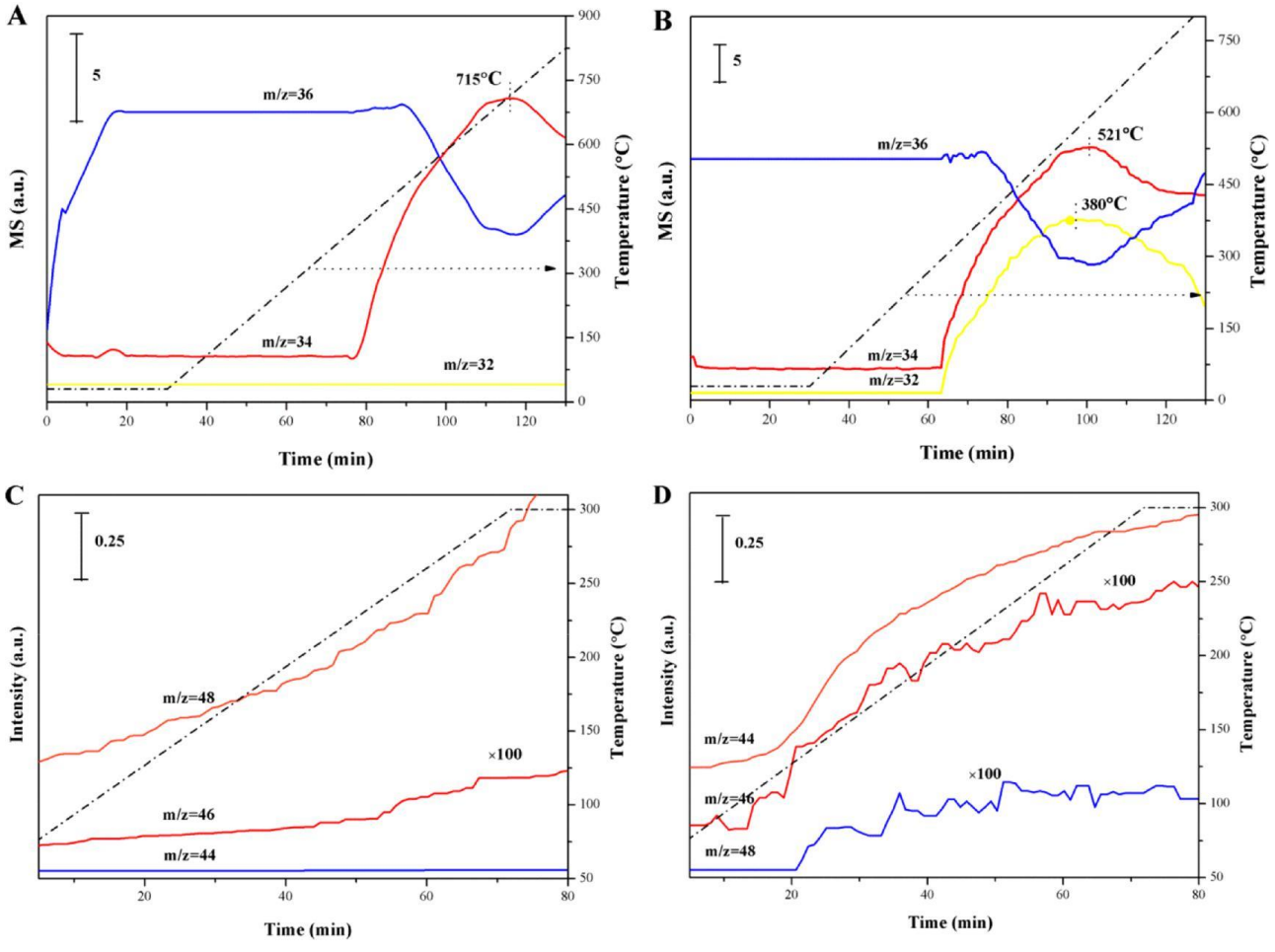

Figure 8. Temperature-programmed isotopic exchange (TPIE) experiment of (A) $Pt_{0.3}/SiO_2$-nc and (B) $Pt_{0.3}Mn_5/SiO_2$-nc. $^{18}O_2$ isotopic exchange studies of (C) $Pt_{0.3}/SiO_2$-nc and (D) $Pt_{0.3}Mn_5/SiO_2$-nc for MEK combustion.

bridging of CO shifts to lower energy (2078 cm^{-1}). Previous work has suggested that a downward shift of this nature can be attributed to the adsorption of CO on large platinum crystallites.[55,56] Given that fully reduced, well dispersed Pt particles are considered to promote catalytic performance in the total oxidation of VOCs, it is somewhat unsurprising that the $Pt_{0.3}Mn_x/SiO_2$-nc materials display such a high performance for the total oxidation of MEK. More metallic Pt nanoparticles were confirmed over $Pt_{0.3}Mn_5/SiO_2$-nc catalyst in comparison with $Pt_{0.3}/SiO_2$-nc, which is ascribed to the transfer of electrons from Mn^{3+} to Pt^{2+} via conjugated π bonding from Mn−O−Pt moieties. This, in turn, increases the Pt^0/Pt^{2+} ratio on the surface of the material, which we believe to be ultimately responsible for the enhanced MEK oxidation activity (Figure 4A) and increased stability of these Mn_2O_3-doped Pt-supported materials (Figure 4C and Figure S4).

Additional investigations were subsequently conducted in order to determine the influence in which O_2 has on the combustion of MEK over the materials synthesized in this study. For this, TPSR experiments were performed in air and N_2 and the corresponding results are displayed in Figure S7. These studies indicate that the lattice oxygen plays an important role in MEK combustion. The mobility of lattice oxygen was subsequently evaluated by TPIE (Figure 8A,B) and ^{18}O isotopic studies (Figure 8C,D). Figure 8A,B illustrates that changes in the normalized signals for all three oxygen isotopic species, namely $^{18}O_2$ (m/z 36), $^{16}O^{18}O$ (m/z 34) and $^{16}O_2$ (m/z 32), are observed by a heteroexchange process, which appears to be temperature dependent. A previous study suggested that gas-phase $^{16}O_2$ signals typically arise from multiple hetero-exchange mechanisms between an 18-dioxygen molecule ($^{18}O_2$) and two surface oxygen atoms of the solid ($^{16}O^{16}O$-s).[57] However, it was also suggested that gas-phase $^{16}O^{18}O$ can be produced via a simple heteroexchange mechanism between one ^{18}O atom of the $^{18}O_2$ isotope molecule and one ^{16}O atom of the metal oxide surface.[57] When similar experiments were conducted over the $Pt_{0.3}/SiO_2$-nc material prepared in this study, no signal corresponding to $^{16}O_2$ was observed. However, a broad peak corresponding to $^{16}O^{18}O$ was observed at 430 °C (centered at 715 °C) and a negative peak corresponding to $^{18}O_2$ was observed between 500 and 800 °C. When a similar experiment was conducted over the $Pt_{0.3}Mn_5/SiO_2$-nc catalyst, there were noticeable changes to the profile. Over this material, the negative peak corresponding to the $^{18}O_2$ species appeared at a significantly lower temperature (centered at 512 °C), indicating that oxygen exchange appears to be enhanced when Mn_2O_3 is present on the surface of the catalyst. In addition to this, the formation of $^{16}O_2$ species was also observed (between 290 and 380 °C) over the $Pt_{0.3}Mn_5/SiO_2$-nc catalyst, which further demonstrates the efficient oxygen mobility which occurs in this material.

Figure 8C,D shows how some carbon-containing isotopic species ($C^{18}O_2$, $C^{16}O^{18}O$, and $C^{16}O_2$) are produced over the

$Pt_{0.3}/SiO_2$-nc and $Pt_{0.3}Mn_5/SiO_2$-nc catalysts in the oxidation of MEK. Again, the temperature was varied over the course of the experiment to determine whether the formation of these species was temperature dependent. With the $Pt_{0.3}/SiO_2$-nc catalyst, the relative concentrations of the $C^{18}O_2$ and $C^{16}O\ ^{18}O$ species were found to increase with increasing temperature. No signal corresponding to $C^{16}O_2$ was detected, and the signal corresponding to $C^{18}O_2$ was significantly more intense than the signal attributed to $C^{16}O^{18}O$. This implies that surface-adsorbed oxygen is essential for the combustion of MEK over the $Pt_{0.3}/SiO_2$-nc catalyst. However, the distribution of these isotopes ($C^{18}O_2$, $C^{16}O^{18}O$, and $C^{16}O_2$ species) produced over the $Pt_{0.3}Mn_5/SiO_2$-nc are vastly different. Over the Mn-doped catalyst, $C^{16}O^{18}O$ and $C^{16}O_2$ species were observed at all the investigated temperatures. The intensity of the signal corresponding to these isotopic species appeared to increase with time and, interestingly, no $C^{18}O_2$ appears to be observed until temperatures above 130 °C are used. Given that such large proportions of ^{18}O were incorporated into the reaction products over the $Pt_{0.3}Mn_5/SiO_2$-nc catalyst, this provides further evidence that of the mobility of the lattice oxygen promotes the combustion of MEK over this material. From this investigation, it can be concluded that the contributions of lattice oxygen in the combustion of MEK over $Pt_{0.3}/SiO_2$-nc and $Pt_{0.3}Mn_5/SiO_2$-nc are vastly different. This observed enhancement in oxygen mobility may be a result of the exposed (222) Mn_2O_3 facets in the Mn-doped material. The presence of Pt likely weakens the Mn−O bonds, which ultimately promotes the mobility of lattice oxygen in the $Pt_{0.3}Mn_5/SiO_2$-nc catalyst.[16]

The nature by which a substrate adsorbs to the surface of a catalyst is considered to be a crucial step in most heterogeneous catalysis processes.[58] The adsorption mode and strength by which a substrate adsorbs to a surface can often dictate the activity and selectivity of a given reaction. As such, DFT calculations were conducted in order to investigate the role of the intermediate products anchoring on the catalyst, to provide further insights into how MEK adsorbs on these materials and what combustion pathways occur. The results of these calculations are illustrated in Figure 9 and show that MEK molecules initially adsorb to the $Pt_{0.3}/SiO_2$-nc and $Pt_{0.3}Mn_5/SiO_2$-nc catalysts on bridged sites with corresponding adsorption energies of −1.3 and −1.5 eV, respectively. This indicates that the MEK molecules have a higher affinity to adsorb onto the surface of the $Pt_{0.3}Mn_5/SiO_2$-nc material. Additional calculations revealed that acetone possesses a lower adsorption energy (−0.9 eV) in comparison to 2-butanol (−0.6 eV), indicating that the quantity and strength of the Brønsted acid sites which are enhanced by Mn_2O_3 are beneficial for acetone adsorption and provide a proton to break the C−C bonds. Subsequent calculations revealed that acetaldehyde is likely produced by demethylation from acetone. The adsorption energy of acetaldehyde over the $Pt_{0.3}/SiO_2$-nc material is higher than that calculated over the $Pt_{0.3}Mn_5/SiO_2$-nc catalyst (−0.6 and −0.8 eV, respectively). With the $Pt_{0.3}Mn_5/SiO_2$-nc catalyst, the adsorption energies of the intermediate species appear to decrease the farther you proceed through the oxidation pathway. This trend is not observed with the results from the adsorption calculations conducted over the $Pt_{0.3}/SiO_2$-nc material. As such, it can be concluded that the reaction route of MEK combustion over $Pt_{0.3}Mn_5/SiO_2$-nc is promoted by Mn_2O_3.

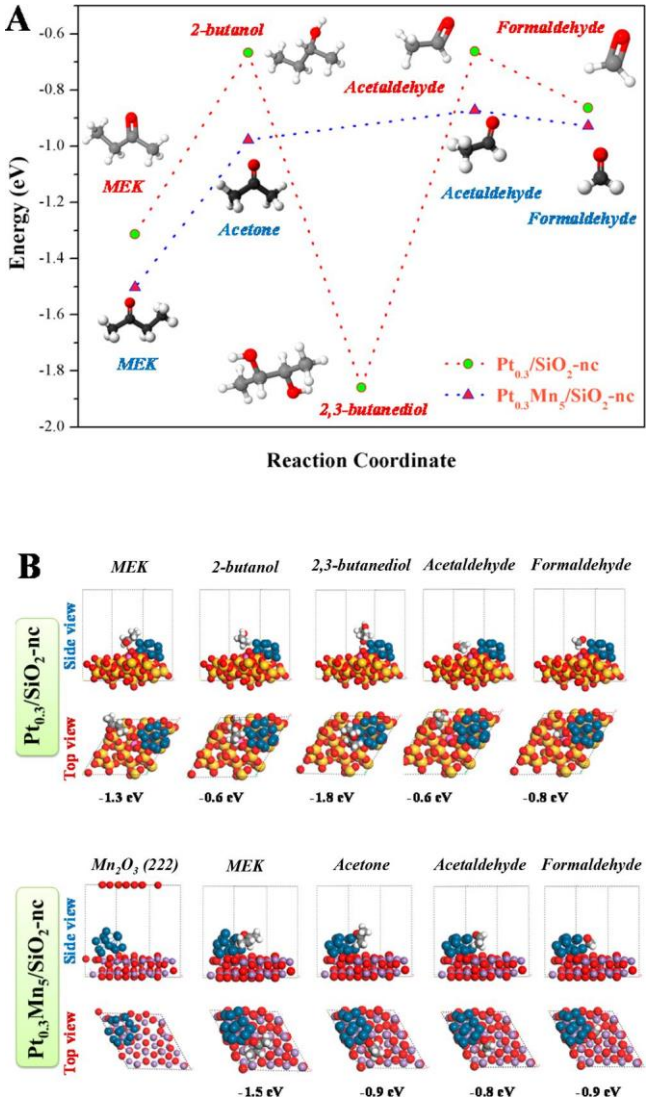

Figure 9. DFT studies of adsorption energy (A) and structure molding for adsorption of key intermediates (B) over $Pt_{0.3}/SiO_2$-nc and $Pt_{0.3}Mn_5/SiO_2$-nc catalysts during MEK oxidation.

A reaction mechanism for the oxidation of MEK over the $Pt_{0.3}/SiO_2$-nc and $Pt_{0.3}Mn_5/SiO_2$-nc catalysts is proposed in Scheme 1, which is based on the conclusions derived from the qualitative and quantitative experiments conducted in this study. Over the $Pt_{0.3}/SiO_2$-nc catalyst, MEK is adsorbed on the surface of the silica support (Figure S6), which is transformed to 2,3-butanediol via 2-butanol a process which is promoted by the presence of surface-adsorbed oxygen (Figure 8). The 2,3-butanediol then undergoes an oxidative cleavage to form acetaldehyde, which ultimately undergoes a sequential oxidation to produce CO_2 and H_2O (Figure 5). Importantly, considering a classical approach for the process of this reaction, the kinetics of the combustion of MEK in air at low concentrations over the $Pt_{0.3}/SiO_2$-nc catalyst is well described by the Langmuir−Hinshelwood (LH) mechanism.[59] The procedure of 2,3-butanediol cleaved to form acetaldehyde is the possible rate-determining step. The difference in proposed surface mechanism for MEK combustion can be confirmed over the $Pt_{0.3}Mn_5/SiO_2$-nc catalyst. The extensive characterizations in this study have shown that the Mn_2O_3 in $Pt_{0.3}Mn_5/SiO_2$-nc material significantly enhances the quantity and strength of the

Scheme 1. Reaction Mechanism for MEK Catalytic Oxidation over $Pt_{0.3}/SiO_2$-nc and $Pt_{0.3}Mn_5/SiO_2$-nc Catalysts

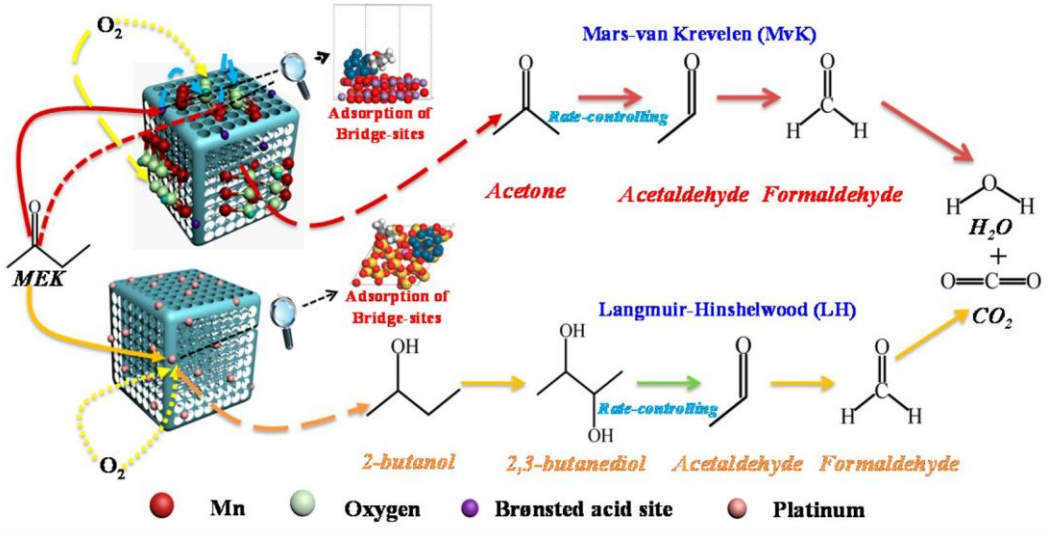

Brønsted acid sites (Figure 6) in this material, and lattice oxygen is incorporated in the reaction products (Figure 8 and Figure S7). The initial step involves the adsorption of MEK over the Brønsted acid sites of the catalyst (Figure S6). MEK is first decomposed to acetone, which is promoted by the protonic donation from the Brønsted acid sites. The acetone subsequently undergoes a similar transformation to acetaldehyde, which further converts to formaldehyde, a process that is again assisted by the Pt active sites. The resulting formaldehyde then undergoes a sequential oxidation to produce CO_2 and H_2O with the help of lattice oxygen (Figure 5). Especially, a classical approach to analyze the kinetics of reactions catalyzed by solids lies in proposing a reaction scheme consisting of a series of steps describing the adsorption of reactants, surface reaction over active sites with lattice oxygen, and product desorption, which is well described by the Mars−van Krevelen mechanism.[60] The lattice oxygen of Mn_2O_3 takes part in the combustion reaction and the oxygen vacancies remain, the latter being replenished by the chemisorbed oxygen. The possible rate-determining step is the process of acetone conversion into acetaldehyde.

CONCLUSIONS

In this work, $Pt_{0.3}Mn_x/SiO_2$ nanocubic (nc) micro-/mesoporous composite materials containing different quantities of Mn were synthesized and utilized as catalysts for the oxidation of methyl ethyl ketone (MEK) for the first time. All of the $Pt_{0.3}Mn_x/SiO_2$-nc materials exhibited an exceptional low-temperature oxidation activity, CO_2 selectivity, and stability for MEK oxidation. Of the catalysts synthesized, the $Pt_{0.3}Mn_5/SiO_2$-nc material was found to be the most active catalyst and could completely oxidize MEK at just 163 °C under a high space velocity of 42600 mL g^{-1} h^{-1}. We believe this to be a new benchmark for low-temperature catalytic oxidation performance for the total oxidation of VOCs. Remarkable synergistic effects between the Pt nanoparticles and the Mn_2O_3 were observed. FTIR spectra corresponding to the adsorption of NH_3 on these materials in combination with a series of TPD experiments confirmed that highly exposed Mn_2O_3 (222) facets enhanced the quantity and strength of the Brønsted acid sites on the surface of these materials. These sites were found to promote the desorption of surface-adsorbed O_2 and CO_2, liberating active sites for MEK molecules to adsorb to. Results from $^{18}O_2$ isotopic exchange and temperature-programmed isotopic exchange experiments revealed that the presence of a Pt−O−Mn moiety weakens the strength of the Mn−O bonds, which promotes the mobility of lattice oxygen in Mn_2O_3. Perhaps most importantly, it was determined that the Mn^{4+}/Mn^{3+} redox cycle in the Mn_2O_3 supplies electrons to Pt sites, which ultimately enhances the proportion of Pt^0/Pt^{2+} on the surface and increases the activity and stability of the catalyst. In situ DRIFTS, online FTIR, and DFT results revealed that acetone and acetaldehyde are the main intermediates produced in the oxidation of MEK over $Pt_{0.3}Mn_5/SiO_2$-nc, which can subsequently undergo further oxidation to H_2O and CO_2 via a formaldehyde intermediate.

ASSOCIATED CONTENT

* Supporting Information

The Supporting Information is available free of charge on the ACS Publications website at DOI: 10.1021/acscatal.7b04461.

Catalyst characterizations, XRD patterns, N_2 adsorption−desorption isotherms and pore size distribution, HAADF-STEM and EDS mapping images, TGA-FTIR analysis, O_2-TPD and CO_2-TPD profiles, TPSR profiles, in situ DRIFTS spectra of MEK adsorption, and summary of some active catalysts for MEK oxidation reported in the literature (PDF)

AUTHOR INFORMATION

Corresponding Authors

*C.H.: tel/fax, +86 29 82663857; e-mail, chi_he@xjtu.edu.cn.

*J.-W.S.: tel/fax, +86 29 83395372; e-mail, jianwen.shi@mail.xjtu.edu.cn .

ORCID

Chi He: 0000-0001-6403-1277

Jian-Wen Shi: 0000-0002-2377-7491

Zhengping Hao: 0000-0003-3400-0220

Notes

The authors declare no competing financial interest.

ACKNOWLEDGMENTS

This work was financially supported by the National Natural Science Foundation of China (21677114, 21477095), the National Key Research and Development Program (2016YFC0204201), and the Fundamental Research Funds for the Central Universities (xjj2017170). Valuable comments from the editor and anonymous reviewers are much appreciated.

REFERENCES

(1) Pan, H.; Jian, Y.; Chen, C.; He, C.; Hao, Z.; Liu, H.; Shen, Z. Sphere-shaped Mn_3O_4 catalyst with remarkable low-temperature activity for methyl-ethyl-ketone combustion. Environ. Sci. Technol. 2017, 51, 6288−6297.

(2) Zhang, C.; Wang, C.; Gil, S.; Boreave, A.; Retailleau, L.; Guo, Y.; Valverde, J. L.; Giroir-Fendle, A. Catalytic oxidation of 1, 2-dichloropropane over supported $LaMnO_X$ oxides catalysts. Appl. Catal., B 2017, 201, 552−560.

(3) Royer, S.; Duprez, D.; Can, F.; Courtois, X.; Batiot-Dupeyrat, C.; Laassiri, S.; Alamdari, H. Perovskites as substitutes of noble metals for heterogeneous catalysis: dream or reality. Chem. Rev. 2014, 114, 10292−10368.

(4) Liotta, L. F. Catalytic oxidation of volatile organic compounds on supported noble metals. Appl. Catal., B 2010, 100, 403−412.

(5) Mistry, H.; Behafarid, F.; Zhou, E.; Ono, L. K.; Zhang, L.; Roldan Cuenya, B. Shape-Dependent Catalytic Oxidation of 2-Butanol over Pt Nanoparticles Supported on γ-Al_2O_3. ACS Catal. 2014, 4, 109−115.

(6) An, K.; Alayoglu, S.; Musselwhite, N.; Plamthottam, S.; Melaet, G.; Lindeman, A. E.; Somorjai, G. A. Enhanced CO oxidation rates at the interface of mesoporous oxides and Pt nanoparticles. J. Am. Chem. Soc. 2013, 135, 16689−16696.

(7) Wang, H.; Lu, Y.; Han, Y.; Lu, C.; Wan, H.; Xu, Z.; Zheng, S. Enhanced catalytic toluene oxidation by interaction between copper oxide and manganese oxide in Cu-O-Mn/γ-Al_2O_3 catalysts. Appl. Surf. Sci. 2017, 420, 260−266.

(8) Qu, Z.; Chen, D.; Sun, Y.; Wang, Y. High catalytic activity for formaldehyde oxidation of AgCo/APTES@ MCM-41 prepared by two steps method. Appl. Catal., A 2014, 487, 100−109.

(9) Li, D.; Yang, G.; Li, P.; Wang, J.; Zhang, P. Promotion of formaldehyde oxidation over Ag catalyst by Fe doped MnO_X support at room temperature. Catal. Today 2016, 277, 257−265.

(10) Cui, W.; Yuan, X.; Wu, P.; Zheng, B.; Zhang, W.; Jia, M. Catalytic properties of γ-Al_2O_3 supported Pt-FeO_X catalysts for complete oxidation of formaldehyde at ambient temperature. RSC Adv. 2015, 5, 104330−104336.

(11) Vít, Z.; Gulková, D.; Kaluža, L.; Boaro, M. Effect of catalyst precursor and its pretreatment on the amount of β-Pd hydride phase and HDS activity of Pd-Pt/silica-alumina. Appl. Catal., B 2014, 146, 213−220.

(12) He, C.; Zhang, F.; Yue, L.; Shang, X.; Chen, J.; Hao, Z. Nanometric palladium confined in mesoporous silica as efficient catalysts for toluene oxidation at low temperature. Appl. Catal., B 2012, 111−112, 46−57.

(13) He, C.; Zhang, X.; Gao, S.; Chen, J.; Hao, Z. Nanometric Pd-confined mesoporous silica as high-efficient catalyst for toluene low temperature removal: Effects of support morphology and textural property. J. Ind. Eng. Chem. 2012, 18, 1598−1605.

(14) Scire, S.; Liotta, L. F. Supported gold catalysts for the total oxidation of volatile organic compounds. Appl. Catal., B 2012, 125, 222−246.

(15) Jiang, Y.; Xie, S.; Yang, H.; Deng, J.; Liu, Y.; Dai, H. Mn_3O_4-Au/3DOM $La_{0.6}Sr_{0.4}CoO_3$: High-performance catalysts for toluene oxidation. Catal. Today 2017, 281, 437−446.

(16) O Shea, V. A. d. l. P.; Alvarez-Galvan, M. C.; Fierro, J. L. G.; Arias, P. L. Influence of feed composition on the activity of Mn and PdMn/Al_2O_3 catalysts for combustion of formaldehyde/methanol. Appl. Catal., B 2005, 57, 191−199.

(17) Colman-Lerner, J. E.; Peluso, M. A.; Sambeth, J. E.; Thomas, H. J. Volatile organic compound removal over bentonite-supported Pt, Mn and Pt/Mn monolithic catalysts. React. Kinet., Mech. Catal. 2013, 108, 443−458.

(18) Xie, Y.; Yu, Y.; Gong, X.; Guo, Y.; Guo, Y.; Wang, Y.; Lu, G. Effect of the crystal plane figure on the catalytic performance of MnO_2 for the total oxidation of propane. CrystEngComm 2015, 17, 3005−3014.

(19) Arzamendi, G.; Pena OShea, V. A. d. l. P.; Alvarez-Galvan, M. C.; Fierro, J. L. G.; Arias, P. L.; Gandía, L. M. Kinetics and selectivity of methyl-ethyl-ketone combustion in air over alumina-supported PdO_X−MnO_X catalysts. J. Catal. 2009, 261, 50−59.

(20) Wang, X.; Zhang, Y.; Luo, W.; Elzatahry, A. A.; Cheng, X.; Alghamdi, A.; Abdullah, A. M.; Deng, Y.; Zhao, D. Synthesis of ordered mesoporous silica with tunable morphologies and pore sizes via a nonpolar solvent-assisted stober method. Chem. Mater. 2016, 28, 2356−2362.

(21) Bai, B.; Qiao, Q.; Arandiyan, H.; Li, J.; Hao, J. Three-dimensional ordered mesoporous MnO_2-supported Ag nanoparticles for catalytic removal of formaldehyde. Environ. Sci. Technol. 2016, 50, 2635−2640.

(22) Kozuch, S.; Martin, J. M. L. Turning over" definitions in catalytic cycles. ACS Catal. 2012, 2, 2787−2794.

(23) Çelik, B.; Erken, E.; Eriş, S.; Yıldız, Y.; Şahin, B.; Pamuk, H.; Sen, F. Highly monodisperse Pt(0)@AC NPs as highly efficient and reusable catalysts: the effect of the surfactant on their catalytic activities in room temperature dehydrocoupling of DMAB. Catal. Sci. Technol. 2016, 6, 1685−1692.

(24) Arandiyan, H.; Dai, H.; Ji, K.; Sun, H.; Zhao, Y.; Li, J. Enhanced Catalytic Efficiency of Pt Nanoparticles Supported on 3D Ordered Macro-/Mesoporous $Ce_{0.6}Zr_{0.3}Y_{0.1}O_2$ for Methane Combustion. Small 2015, 11, 2366−2371.

(25) Andrei, R. D.; Popa, M. L.; Fajula, F.; Hulea, V. Heterogeneous oligomerization of ethylene over highly active and stable Ni-AlSBA-15 mesoporous catalysts. J. Catal. 2015, 323, 76−84.

(26) Jiang, Z.; He, C.; Dummer, N. F.; Shi, J.; Tian, M.; Ma, C.; Hao, Z.; Taylor, S. H.; Ma, M.; Shen, Z. Insight into the efficient oxidation of methyl-ethyl-ketone over hierarchically micro-mesostructured Pt/K-(Al)SiO_2 nanorod catalysts: Structure-activity relationships and mechanism. Appl. Catal., B 2018, 226, 220−233.

(27) Kovarik, L.; Washton, N. M.; Kukkadapu, R.; Devaraj, A.; Wang, A.; Wang, Y.; Szanyi, J.; Peden, C. H. F.; Gao, F. Transformation of active sites in Fe/SSZ-13 SCR catalysts during hydrothermal aging: a spectroscopic, microscopic, and kinetics study. ACS Catal. 2017, 7, 2458−2470.

(28) Huang, X.; Men, Y.; Wang, J.; An, W.; Wang, Y. Highly active and selective binary MgO-SiO_2 catalysts for the production of 1, 3-butadiene from ethanol. Catal. Sci. Technol. 2017, 7, 168−180.

(29) Cai, J.; Huang, Y.; Huang, B.; Zheng, S.; Guo, Y. Enhanced activity of Pt nanoparticle catalysts supported on manganese oxide-carbon nanotubes for ethanol oxidation. Int. J. Hydrogen Energy 2014, 39, 798−807.

(30) Yang, T.; Huo, Y.; Liu, Y.; Rui, Z.; Ji, H. Efficient formaldehyde oxidation over nickel hydroxide promoted Pt/γ-Al_2O_3 with a low Pt content. Appl. Catal., B 2017, 200, 543−551.

(31) Chen, C.; Li, B.; Zhou, L.; Xia, Z.; Feng, N.; Ding, J.; Wang, L.; Wan, H.; Guan, G. Synthesis of Hierarchically Structured Hybrid Materials by Controlled Self-Assembly of Metal-Organic Framework with Mesoporous Silica for CO_2 Adsorption. ACS Appl. Mater. Interfaces 2017, 9, 23060−23071.

(32) Lopez-Benítez, A.; Berhault, G.; Guevara-Lara, A. NiMo catalysts supported on Mn-Al_2O_3 for dibenzothiophene hydro-desulfurization application. Appl. Catal., B 2017, 213, 28−41.

(33) Wisniewska, J.; Ziolek, M. Formation of Pt-Ag alloy on different silicas-surface properties and catalytic activity in oxidation of methanol. RSC Adv. 2017, 7, 9534−9544.

(34) Czaplinska, J.; Decyk, P.; Ziolek, M. S. Surface properties and catalytic performance of Pt-Ag supported on silica-The effect of preparation methods. Appl. Catal., A 2015, 504, 361−372.

(35) Tangale, N. P.; Sonar, S. K.; Niphadkar, P. S.; Joshi, P. N. Hierarchical K/LTL zeolites: Synthesis by alkali treatment, character-ization and catalytic performance in Knoevenagel condensation reaction. J. Ind. Eng. Chem. 2016, 40, 128−136.

(36) Wang, C.; Zhang, C.; Hua, W.; Guo, Y.; Lu, G.; Gil, S.; Giroir-Fendler, A. Catalytic oxidation of vinyl chloride emissions over Co-Ce composite oxide catalysts. Chem. Eng. J. 2017, 315, 392−402.

(37) Si, W.; Wang, Y.; Zhao, S.; Hu, F.; Li, J. A facile method for in situ preparation of the MnO_2/$LaMnO_3$ catalyst for the removal of toluene. Environ. Sci. Technol. 2016, 50, 4572−4578.

(38) He, C.; Yu, Y.; Shen, Q.; Chen, J.; Qiao, N. Catalytic behavior and synergistic effect of nanostructured mesoporous CuO-MnO_x-CeO_2 catalysts for chlorobenzene destruction. Appl. Surf. Sci. 2014, 297, 59−69.

(39) You, H.; Zhang, F.; Liu, Z.; Fang, J. Free-standing Pt-Au hollow nanourchins with enhanced activity and stability for catalytic methanol oxidation. ACS Catal. 2014, 4, 2829−2835.

(40) Zhao, H.; Wang, D.; Gao, C.; Liu, H.; Han, L.; Yin, Y. Ultrafine platinum/iron oxide nanoconjugates confined in silica nanoshells for highly durable catalytic oxidation. J. Mater. Chem. A 2016, 4, 1366− 1372.

(41) Yan, Z.; Xu, Z.; Yu, J.; Jaroniec, M. Highly active mesoporous ferrihydrite supported Pt catalyst for formaldehyde removal at room temperature. Environ. Sci. Technol. 2015, 49, 6637−6644.

(42) Zou, X.; Rui, Z.; Song, S.; Ji, H. Enhanced methane combustion performance over $NiAl_2O_4$-interface-promoted Pd/γ-Al_2O_3. J. Catal. 2016, 338, 192−201.

(43) Zhang, R.; Shi, D.; Liu, N.; Cao, Y.; Chen, B. Mesoporous SBA-15 promoted by 3d-transition and noble metals for catalytic combustion of acetonitrile. Appl. Catal., B 2014, 146, 79−93.

(44) Lai, Y. T.; Chen, T. C.; Lan, Y. K.; Chen, B. S.; You, J. H.; Yang, C. M.; Lai, N. C.; Wu, J. H.; Chen, C. S. Pt/SBA-15 as a highly efficient catalyst for catalytic toluene oxidation. ACS Catal. 2014, 4, 3824−3836.

(45) Chen, C. S.; Lai, Y. T.; Chen, T. C.; Chen, C. H.; Lee, J. F.; Hsu, C. W.; Kao, H. M. Synthesis and characterization of Pt nanoparticles with different morphologies in mesoporous silica SBA-15 for methanol oxidation reaction. Nanoscale 2014, 6, 12644−54.

(46) Yao, X.; Kong, T.; Yu, S.; Li, L.; Yang, F.; Dong, L. Influence of different supports on the physicochemical properties and denitration performance of the supported Mn-based catalysts for NH_3-SCR at low temperature. Appl. Surf. Sci. 2017, 402, 208−217.

(47) Tang, C.; Zhai, Z.; Li, X.; Sun, L.; Bai, W. Highly efficient and robust $Mg_{0.388}Al_{2.408}O_4$ catalyst for gas-phase decarbonylation of lactic acid to acetaldehyde. J. Catal. 2015, 329, 206−217.

(48) Zhang, Q.; Tan, Y.; Liu, G.; Zhang, J.; Han, Y. Rhenium oxide-modified $H_3PW_{12}O_{40}$/TiO_2 catalysts for selective oxidation of dimethyl ether to dimethoxy dimethyl ether. Green Chem. 2014, 16, 4708−4715.

(49) She, X. Y.; Kwak, J. H.; Sun, J. M.; Hu, J. Z.; Hu, M. Y.; Wang, C. M.; Peden, C. H. F.; Wang, Y. Highly Dispersed and Active ReO_x on Alumina-Modified SBA-15 Silica for 2-Butanol Dehydration. ACS Catal. 2012, 2, 1020−1026.

(50) Wu, H.-C.; Chen, T.-C.; Lai, N.-C.; Yang, C.-M.; Wu, J.-H.; Chen, Y.-C.; Lee, J.-F.; Chen, C.-S. Synthesis of sub-nanosized Pt particles on mesoporous SBA-15 material and its application to the CO oxidation reaction. Nanoscale 2015, 7, 16848−16859.

(51) Shen, S.; Wang, X.; Ding, Q.; Jin, S.; Feng, Z.; Li, C. Effect of Pt cocatalyst in Pt/TiO_2 studied by in situ FTIR of CO adsorption. Chin. J. Catal. 2014, 35, 1900−1906.

(52) Rizo, R.; Sebastian,́D.; Rodríguez, J. L.; Lazaro,́ M. J.; Pastor, E. Influence of the nature of the carbon support on the activity of Pt/C catalysts for ethanol and carbon monoxide oxidation. J. Catal. 2017, 348, 22−28.

(53) Wan, J.; Ran, R.; Lin, M.; Wu, X.; Weng, D. Effect of acid and base modification on the catalytic activity of Pt/Al2O3 for propene oxidation. J. Mol. Catal. A: Chem. 2014, 383−384, 194−202.

(54) Farias, M. J. S.; Buso-́Rogero, C.; Gisbert, R.; Herrero, E.; Feliu, J. M. Influence of the CO adsorption environment on its reactivity with (111) terrace sites in stepped Pt electrodes under alkaline media. J. Phys. Chem. C 2014, 118, 1925−1934.

(55) Wisniewska, J.; Ziolek, M.; Artioli, N.; Daturi, M. The effect of niobium and tantalum on physicochemical and catalytic properties of silver and platinum catalysts based on MCF mesoporous cellular foams. J. Catal. 2016, 336, 58−74.

(56) Kale, M. J.; Christopher, P. Utilizing quantitative in situ FTIR spectroscopy to identify well-coordinated Pt atoms as the active site for CO oxidation on Al_2O_3-supported Pt catalysts. ACS Catal. 2016, 6, 5599−5609.

(57) Choi, S. O.; Penninger, M.; Kim, C. H.; Schneider, W. F.; Thompson, L. T. Experimental and Computational Investigation of Effect of Sr on NO Oxidation and Oxygen Exchange for $La_{1-x}Sr_xCoO_3$ Perovskite Catalysts. ACS Catal. 2013, 3, 2719−2728.

(58) Yan, L.; Liu, Y.; Zha, K.; Li, H.; Shi, L.; Zhang, D. Scale−Activity Relationship of MnO_x-FeO_y Nanocage Catalysts Derived from Prussian Blue Analogues for Low-Temperature NO Reduction: Experimental and DFT Studies. ACS Appl. Mater. Interfaces 2017, 9, 2581−2593.

(59) Zasada, F.; Janas, J.; Piskorz, W.; Gorczynska, M.; Sojka, Z. Total Oxidation of Lean Methane over Cobalt Spinel Nanocubes Controlled by the Self-Adjusted Redox State of the Catalyst: Experimental and Theoretical Account for Interplay between the Langmuir-Hinshelwood and Mars-Van Krevelen Mechanisms. ACS Catal. 2017, 7, 2853−2867.

(60) Kim, H. Y.; Henkelman, G. CO Oxidation at the Interface of Au Nanoclusters and the Stepped-CeO_2(111) Surface by the Mars-van Krevelen Mechanism. J. Phys. Chem. Lett. 2013, 4, 216−221.